FEDERAL UNIVERSITY OF SANTA CATARINA
TECHNOLOGICAL CENTER
DEPARTMENT OF CHEMICAL AND FOOD ENGINEERING

Natan Padoin

CONTRIBUTIONS TO PROCESS INTENSIFICATION IN MICROFLUIDIC DEVICES

Florianópolis
2016

Natan Padoin

CONTRIBUTIONS TO PROCESS INTENSIFICATION IN MICROFLUIDIC DEVICES

Doctorate thesis for the degree of Doctor in Chemical Engineering presented to the Graduate Program in Chemical Engineering at Federal University of Santa Catarina.

Advisor: Prof. Dr. Cíntia Soares

Florianópolis
2016

Padoin, Natan
Contributions to Process Intensification in Microfluidic Devices / Natan Padoin ; orientadora, Cíntia Soares - Florianópolis, SC, 2016.
116 p.

Tese (doutorado) - Universidade Federal de Santa Catarina, Centro Tecnológico. Programa de Pós-Graduação em Engenharia Química.

Inclui referências

1. Engenharia Química. 2. Microfluidics. 3. Process intensification. 4. Photocatalysis. 5. Computational modeling. I. Soares, Cíntia. II. Universidade Federal de Santa Catarina. Programa de Pós-Graduação em Engenharia Química. III. Título.

Natan Padoin

CONTRIBUTIONS TO PROCESS INTENSIFICATION IN MICROFLUIDIC DEVICES

This thesis was considered adequate for the degree of Doctor in Chemical Engineering and was approved in its final form by the Graduate Program in Chemical Engineering at Federal University of Santa Catarina.

Florianópolis, December 14th 2016.

_____
Prof. Cíntia Soares, Dr.
Coordinator of the Graduate Program in Chemical Engineering

Examination Board:

_____
Prof. Henry França Meier, Dr.
University of Blumenau – FURB

_____
Prof. Márcio Antônio Fiori, Dr.
University of Chapecó – UNOCHAPECÓ

_____
Prof. Alexandre Kupka da Silva, Dr.
Federal University of Santa Catarina – UFSC

_____
Prof. Luismar Marques Porto, Dr.
Federal University of Santa Catarina – UFSC

_____
Prof. Regina de F. P. M. Moreira, Dr.
Federal University of Santa Catarina – UFSC

To all dreamers.

ACKNOWLEDGEMENTS

First of all, I would like to thank my family for the everyday inspiration.

I would like to specially thank my advisor, Prof. Dr. Cíntia Soares, for the friendship, for the opportunities and for her confidence in this work. You have inspired me to be a better person every day. Thank you for being this great person.

I am grateful to the Laboratory of Energy and the Environment (LEMA-UFSC), specially to Prof. Regina de Fátima Peralta Muniz Moreira and Prof. Humberto Jorge José, for the valuable support for this research.

I also thank all my colleagues that somehow have inspired me to make this research real.

I would like to acknowledge Federal University of Santa Catarina (UFSC), in particular to those involved with the Graduate Program in Chemical Engineering (PósENQ), for the relevant support that was offered along the last years.

I am grateful to my colleagues and supervisors (Dr. Luísa Manuela Madureira Andrade Silva and Prof. Adélio Miguel Magalhães Mendes) at University of Porto, Portugal, for the valuable support provided during my doctoral internship as part of the activities of project CAPES/FCT 347/2013.

Finally, I would like to thank CNPq (National Council for Scientific and Technological Development) and CAPES (Coordination for the Improvement of Higher Education Personnel) for the scholarships.

The designs we see in nature are not the result of chance. They rise naturally, spontaneously, because they enhance access to flow…
(Adrian Bejan)

ABSTRACT

In this work, answers to some gaps found in the literature on the field of process intensification in microfluidic devices were proposed. The behavior of a carbon-based composite photocatalyst, specifically a composite of TiO_2 and graphene, immobilized on the inner walls of a microchannel reactor, was evaluated and compared with a system containing pristine TiO_2. Additionally, a comprehensive computational simulation was performed, based on fundamental physics of semiconductors and considering the coupling of radiation distribution, fluid flow, mass transport and chemical reactions. Moreover, a numerical study was carried out aiming to determine optimal photocatalytic film thicknesses for different illumination mechanisms (backside illumination, BSI, and front-side illumination, FSI) as a function of relevant operational variables and parameters, namely the incident irradiation, the apparent first-order reaction constant, the effective diffusivity and the absorption coefficient. Finally, the possibility of numerically predict the effect of wall wettability on gas-liquid flow pattern developed in microfluidic devices was investigated.

Keywords: Microfluidics. Process intensification. Photocatalysis. Computational modeling.

RESUMO ESTENDIDO

Dispositivos microfluídicos são baseados em microcanais nos quais o diâmetro efetivo é da ordem de centenas de micrômetros, resultando em elevada razão área/volume. Embora um considerável avanço tenha sido observado nessa área nas últimas décadas, resultando, inclusive, em aplicações industriais comercialmente disponíveis, ainda há importantes questões em aberto. Neste trabalho, respostas a algumas dessas questões foram propostas. Em particular, procurou-se determinar o comportamento de dispositivos microfluídicos aplicados à intensificação de processos fotocatalíticos considerando um fotocatalisador compósito (especificamente um compósito de dióxido de titânio e grafeno) imobilizado nas paredes internas. Tal sistema foi, então, comparado a um equivalente no qual dióxido de titânio puro foi imobilizado. As partículas de dióxido de titânio e do compósito de dióxido de titânio-grafeno foram depositadas por meio de um método térmico. Suspensões de TiO_2 e TiO_2-grafeno foram preparadas e injetadas ao longo de microcanais de chips microfluídicos comerciais construídos com vidro borossilicato. Os dispositivos foram, então, tratados termicamente para promover a evaporação do solvente (água) e a deposição do fotocatalisador nas paredes internas. O processo foi realizado ciclicamente para promover a formação de múltiplas camadas. A evolução da deposição foi avaliada pelo monitoramento dos perfis óticos dos sistemas. Azul de metileno foi usado como reagente modelo em ensaios de fotodegradação. Ensaios preliminares permitiram determinar o efeito dos fenômenos de adsorção e fotólise sobre o comportamento global. Nos experimentos de reação fotocatalisada observou-se que uma maior velocidade de reação inicial foi obtida no microrreator contendo fotocatalisador composto (TiO_2-GR) imobilizado nas paredes internas, mas ambos os sistemas (TiO_2 e TiO_2-GR) exibiram velocidades de reação similares quando o estado estacionário foi alcançado. Verificou-se que a taxa de descolorização do azul de metileno no chip microfluídico foi, aproximadamente, uma ordem de magnitude maior que aquela reportada em sistemas macroscópicos equivalentes em condições experimentais similares. Além disso, investigou-se, neste trabalho, a possibilidade de avaliar teoricamente o comportamento de sistemas microfluídicos aplicados a processos fotocatalíticos com base na física fundamental de semicondutores, bem como a possibilidade de modelar computacionalmente os fenômenos acoplados (distribuição de intensidade luminosa, escoamento, transporte de massa e reação química) que ocorrem em reatores de microcanais

(provendo uma estimativa para o desempenho do reator, dos pontos de vista global e local). O modelo computacional foi validado com os resultados experimentais. Na sequência, o modelo computacional foi aplicado para a predição da melhor espessura para o filme fotocatalítico imobilizado nas paredes internas de dispositivos microfluídicos em diferentes condições de iluminação (backside illumination, BSI, e front-side illumination, FSI) como função de variáveis operacionais e parâmetros relevantes, nomeadamente a irradiação incidente, a constante de velocidade de reação aparente de pseudo-primeira ordem, a difusividade efetiva e o coeficiente de absorção do fotocatalisador. Finalmente, a possibilidade de predizer numericamente o efeito da molhabilidade da parede sobre padrões de escoamento multifásicos desenvolvidos em microcanais foi avaliada. Tal modelo computacional pode ser utilizado como fonte de informação prévia sobre o impacto de diferentes propriedades do filme fotocatalítico na morfologia interfacial de escoamento gás-líquido em microrreatores fotoquímicos. Em particular, escoamentos gás-líquido isotérmicos (Taylor e estratificado) foram avaliados através do modelo *volume of fluid* (VOF). Microcanais com condições limites de hidrofilicidade e hidrofobicidade foram investigados tomando-se como base um referencial experimental disponível na literatura. Um estudo preliminar detalhado foi conduzido para a determinação da malha computacional ótima, capaz de permitir modelagem adequada do filme líquido formado entre as cavidades de gás e a parede sólida, no caso de Taylor flow. Os resultados numéricos foram comparados com dados experimentais (comprimento máximo de cavidade e área de cavidade, para o caso de Taylor flow, e espessura do filme gasoso no caso de escoamento estratificado) e algumas correlações disponíveis (comprimento máximo de cavidade e perda de carga por cavidade) e boa concordância foi observada. Nas mesmas condições de alimentação, o modelo foi capaz de captar os diferentes padrões de escoamento gás-líquido esperados quando o ângulo de contato da parede foi variado. Portanto, tal modelo computacional pode ser utilizado em estudos de *scale out* com o objetivo de projetar e otimizar reatores compactos modulares baseados na tecnologia de microcanais nos quais escoamento multifásico, particularmente gás e líquido, é estabelecido. Discussões acerca das limitações e de propostas futuras referentes ao desenvolvimento deste trabalho também são apresentadas.

Palavras-Chave: Microfluídica. Intensificação de processos. Fotocatálise. Modelagem computacional.

LIST OF FIGURES

LIST OF TABLES

LIST OF ABBREVIATIONS

CB	Conduction band
VB	Valence band
E_{BG}	Bandgap energy
Red	Reduction
Ox	Oxidation
e^-	Electron
h^+	Hole
GR	Graphene

LIST OF SYMBOLS

α	Optical absorption coefficient (m^{-1})
δ	Film thickness (m)
δ_H	Hydrodynamic boundary layer thickness (m)
δ_M	Mass boundary layer thickness (m)
ε	Film porosity (dimensionless)
ϕ	Thiele modulus (dimensionless)
γ	Electron transfer coefficient (dimensionless)
κ_λ	Absorption coefficient at wavelength λ (m^{-1})
λ	Wavelength (nm)
μ	Dynamic viscosity ($kg \cdot m^{-1} \cdot s^{-1}$)
η	Effectiveness factor (dimensionless)
ρ	Density ($kg \cdot m^{-3}$)
σ_λ	Scattering coefficient at wavelength λ (m^{-1})
τ	Residence time (s)
τ'	Catalyst tortuosity (dimensionless)
Ω	Angular coordinates
A	Absorbance (dimensionless)
	Photocatalytic film cross-section area (m^2)
Bp_0n_0	Electron/hole recombination equilibrium ($m^3 \cdot s^{-1}$)
C	Methylene blue concentration ($mg \cdot L^{-1}$)
ci	Concentration of species I ($mg \cdot L^{-1}$)
C_0	Initial methylene blue concentration ($mg \cdot L^{-1}$)
$c_{0,i}$	Initial concentration of species I ($mg \cdot L^{-1}$)
D	Diffusion coefficient ($m^{-2} \cdot s^{-1}$)
D_i	Molecular diffusion coefficient of species i ($m^{-2} \cdot s^{-1}$)
D_{eff}	Effective diffusion coefficient ($m^{-2} \cdot s^{-1}$)
$\boldsymbol{F}$	Body forces ($N \cdot m^{-3}$)
$\hbar\omega$	Photon energy (J)
$\boldsymbol{I}$	Identity matrix (dimensionless)
I	Irradiance ($W \cdot m^{-2}$)
I_0	Incident light intensity ($W \cdot m^{-2}$)
I_0^{eff}	Effective incident light intensity ($W \cdot m^{-2}$)
I_λ	Light irradiance at wavelength λ ($W \cdot m^{-2}$)
I_{avg}	Average light intensity ($W \cdot m^{-2}$)
i	Species (dimensionless)
ID	Internal diameter (m)

k	Volumetric reaction rate constant (s^{-1})
k_{app}	Apparent first-order volumetric reaction rate constant (s^{-1})
$k_{r,app}$	
k''_{app}	Apparent first-order superficial reaction rate constant ($m \cdot s^{-1}$)
k_c	Convective mass transfer coefficient ($m \cdot s^{-1}$)
L	Length (m)
	Photocatalytic film total width (m)
LD	Light dependent
$\boldsymbol{n}$	Normal vector (dimensionless)
$\boldsymbol{N_i}$	Diffusive flux of species i ($mol \cdot m^{-2} \cdot s^{-1}$)
$p(\Omega' \rightarrow \Omega)$	Transfer function
r	Reaction rate of species I ($mol \cdot m^{-3} \cdot s^{-1}$)
R	Volumetric reaction rate ($mol \cdot m^{-3} \cdot s^{-1}$)
$-r_A$	Reaction rate ($g \cdot m^{-3} \cdot s^{-1}$)
s	Spatial coordinates (m)
p	Pressure (Pa)
t	Time (s)
T	Transmittance (dimensionless)
T'	Transpose operator (dimensionless)
$\boldsymbol{u}$	Velocity vector ($m \cdot s^{-1}$)
u_0	Velocity at the flow channel inlet ($m \cdot s^{-1}$)
y, x	Cartesian coordinates (m)

CONTENTS

1. WHAT IS THIS THESIS ABOUT?

For a long time, the study of the transport phenomena and chemical reactions at interfaces has been at the core of Chemical Engineering. In fact, at the thin region that separates gas/solid, liquid/solid, gas/liquid and liquid/liquid interfaces all relevant phenomena take place. That is the key concept of the boundary layer theory[1] that has been at the foundation of this discipline.

Therefore, taking into account this scenario, it is clear that eliminating bulk contribution may be beneficial for the maximization of the system performance. In this case, heat and mass transfer rates are enhanced. Consequently, chemical reaction rates are favored. Then, a condition in which the process is intensified is reached.

In fact, several strategies have been developed for the intensification of chemical processes along the last decades. It is possible to consider in this regard the development of structured bed for separation processes in distillation and absorption columns, for instance, where there is a considerable increment in the surface-to-volume ratio. By the way, this parameter (surface-to-volume ratio) is determinant for the maximization of the interfacial effects in any process. So, looking carefully to this direction is of paramount importance if one wants to intensify physical-chemical operations. Recently, the application of microfluidics has emerged as an interesting route in this regard.

In general words, microfluidics deals with the conduction of flow processes in a controlled environment in which the importance of interface relative to the bulk contribution is exceptionally high. Microfluidic systems are basically devices based on microchannels in which the effective diameter is at the range of a few hundreds of micrometers, resulting in surface-to-volume ratios in the order of thousands of square meters per cubic meter. Typically, values as high as $\sim 10^4$ m^2/m^3 are obtained, which represent a substantial gain compared with the scenario observed in traditional equipment used in chemical processes.

It should be highlighted here that Nature has successfully used this concept to provide efficient means for flowing material and energy

[1] The boundary layer is a region which extends from a surface up to the point that corresponds to free stream conditions. Profiles of velocity, temperature and concentration can be found in this region. Outside it (i.e., at the bulk) there are no variations in velocity, temperature and concentration. Therefore, the boundary layer may be recognized as the region in which most of the relevant transport phenomena occur.

through the most diverse structures, spanning from animal circulatory system to vegetal transport networks. In addition, it is relevant to mention that modern theories that aim to explain design in Nature, especially the Constructal Law developed by professor Adrian Bejan (BEJAN and LORENTE, 2013; BEJAN, 2016), are surrounded by this concept. In fact, one can argue that the use of microchannels for process intensification is a direct consequence of the postulates of the Constructal Law. Microfluidic devices are, according to this theory, an evolution regarding macro-sized devices (due to the higher surface-to-volume achieved). According to Bejan (2016), there is a natural tendency of evolution "toward greater density of volumetric flow", or greater density of "functionality", in any technological device.

Typically, devices created with microchannel technology are designed based on unitary elements, which may be replicated to adequate the capacity to real applications. Once the unitary element is optimized and all physics and chemistry that take place inside it are well characterized, one can then parallelize the system in a way that each unit perform essentially identically. Thus, there is a shift from a *scale up* procedure, adopted in the design of conventional equipment for industrial applications, to *scale out* strategies, considering the above-mentioned plan.

Microfluidic devices are, therefore, *a priori* more efficient than the corresponding conventional equipment, due to the intensification of mass and energy transport and chemical reactions through minimization of bulk contribution relative to interface available for changes, and allow easier configuration for any production scale requirement.

Therefore, there is a growing interest in applying microfluidics in several areas, including chemical processing (chemical reaction, distillation, absorption, extraction, etc.). Microreactors, for instance, have been applied for the conduction of Fischer-Tropsch synthesis (conversion of syngas, a mixture of H_2 and CO, to fuels) even in industrial scale. In addition, it is worth to mention that microfluidic devices can be successfully used as sensors and biosensors in several applications, ranging from chemical analysis to medical diagnostics.

In particular, microfluidics may be applied to the intensification of photocatalytic processes. In this case, frequently a photocatalyst (semiconductor) is deposited on the walls of microchannels and the process is carried out continuously, with light (generally in the UV range, i.e. $\lambda < 400$ nm, although recent works have focused on the use of visible radiation) being supplied externally or internally as a photon source for the catalyst activation.

Some works have been published dealing with intensification of photocatalytic processes in microchannels. However, there are, to the best of our knowledge, no contributions reported so far in the literature covering aspects such as the use of composite photocatalysts, specifically TiO_2-graphene, apart of the pristine TiO_2 usually used, a comprehensive modeling of the flow chemistry in these devices, taking into account the fully coupled interaction between light distribution, fluid flow, mass transport and chemical reactions, an explicit optimization of the photocatalyst film thickness that should be deposited on the microchannel walls and a numerical investigation of the effect of varying wettability due to different catalyst washcoats on fluid flow in microreactors, in particular considering a scenario of multiphase flow.

1.1 AIMS OF THIS STUDY

Based on the scenario aforementioned, this thesis aims to provide contributions to the field of photochemical microfluidics giving answers to gaps found in the literature. In particular, answers to the following questions were proposed:

- What is the behavior of microfluidic devices applied to the intensification of photocatalytic processes when considering composite photocatalyst attached on the active walls? When using a composite of TiO_2 and graphene, in particular, how it performs when compared to systems with pristine TiO_2 used as photocatalyst?
- Is it possible to investigate theoretically the behavior of microfluidic systems applied to photocatalytic processes based on fundamental physics of semiconductors? Would it be possible to successfully computationally model the coupled phenomena, i.e., radiation distribution, fluid flow, mass transport and chemical reactions, that occur in microchannel reactors (providing an estimative of the reactor performance, globally and locally)?
- Would it be possible to find an explicit function of optimal photocatalyst film thickness to be deposited on the walls of microfluidic devices considering relevant variables that govern the system dynamics?
- Is it possible to computationally model the effect of the wall wettability on the flow pattern developed in microchannels so

that one could predict the behavior of different washcoats on possible multiphase flow applications in photocatalytic processes carried out in microfluidic devices?

All questions raised are relevant for the advancement of the field of photochemical microfluidics and were not provided in the literature so far. Thus, this work intends to contribute to this field proposing answers to such gaps.

1.2 STRUCTURE OF THIS DOCUMENT

This thesis is organized as follows:

In Chapter 1 the problem is contextualized. General aspects about the questions that this thesis aimed to answer and the results derived from this work are presented and discussed.

In Chapter 2 an experimental and numerical investigation of a photocatalytic process in microchannel reactor is presented. This chapter is based on the article entitled "Intensification of photocatalytic pollutant abatement in microchannel reactor using TiO_2 and TiO_2-graphene", by Natan Padoin, Luísa Andrade, Joana Ângelo, Adélio Mendes, Regina de Fátima Peralta Muniz Moreira and Cíntia Soares, published in *AIChE Journal* (v. 62, n. 8, p. 2794-2802, 2016). The experimental part of this chapter was carried out by the author of this thesis at the Faculty of Engineering of the University of Porto (FEUP), Porto/Portugal, within LEPABE (Laboratory for Process Engineering, Environment, Biotechnology and Energy), in the context of the project CAPES/FCT 347/2013. Moreover, the computational simulations were performed at Federal University of Santa Catarina (UFSC), Florianópolis/Brazil, within LEMA (Laboratory of Energy and the Environment), supported by project CNPq/459299/2014-0 entitled "μPhoto: New Routes for Photocatalytic Pollutant Abatement". The research reported herein consists in the core of this thesis and concerns about the investigation of the decolourization of methylene blue in a microfluidic chip with TiO_2 and TiO_2-graphene immobilized on its inner walls. As mentioned in the original published paper, the content of this chapter distinguishes from the published literature in the area of photocatalytic pollutant abatement in microreactors by the investigation of the possibility of using a composite photocatalyst washcoat, which can be further optimized for sunlight harvesting, and the comprehensive computational modeling of the process herein studied, through coupled radiation distribution within

the catalyst film and reactive flow based on fundamental physics of semiconductors.

In Chapter 3, a numerical optimization of photocatalyst film thickness immobilized in microfluidic devices was carried out. This chapter is based on the article entitled "An explicit correlation for optimal TiO_2 film thickness in immobilized photocatalytic reaction systems", by Natan Padoin and Cíntia Soares, published in *Chemical Engineering Journal* (Volume 310, Part 2, 15 February 2017, Pages 381–388). The research reported in this chapter was entirely conducted at Federal University of Santa Catarina (UFSC), Florianópolis/Brazil, within LEMA, supported by project CNPq/459299/2014-0 entitled "μPhoto: New Routes for Photocatalytic Pollutant Abatement". Different light irradiation schemes were evaluated, namely the backside illumination (BSI) and front-side illumination (FSI) mechanisms, and explicit equations for the prediction of the optimal film thickness as a function of the incident irradiation, the apparent first-order reaction constant, the effective diffusivity and the absorption coefficient were proposed. These equations could be used for optimal design of unitary microfluidic photocatalytic reactors and further *scale out*. Although other works published deal with phenomenological investigation of illumination mechanisms in immobilized photocatalytic systems, this work proposes direct relations (algebraic equations) of optimal film thickness and relevant variables, which was not reported so far.

In Chapter 4, a computational study of the effect of wall wettability on the flow pattern developed in microfluidic devices was conducted. This chapter is based on the article entitled "Numerical simulation of isothermal gas-liquid flow patterns in microchannels with varying wettability", by Natan Padoin, Alan Zago de Souza, Karoline Ropelato and Cíntia Soares, published in *Chemical Engineering Research & Design* (v. 109, n. 1, p. 698-706, 2016). To be as generic as possible, extreme conditions of highly wettable and highly non-wettable walls were evaluated and isothermal gas-liquid flow was considered. The numerical simulations were validated with experimental data previously published (from independent groups). The research reported in this chapter was also entirely conducted at Federal University of Santa Catarina (UFSC), Florianópolis/Brazil, supported by project CNPq/459299/2014-0 entitled "μPhoto: New Routes for Photocatalytic Pollutant Abatement". It should be highlighted that the predictability of flow patterns developed in microchannels under different surface wettability is important since different catalysts may significantly alter the

hydrophobicity/hydrophilicity of the channel walls, which, as demonstrated, will result in very different flow patterns, with consequent variation in interfacial area for momentum and mass transfer (in the case of photocatalytic processes; heat effects should also be considered in the case of thermochemical systems).

Chapter 5 presents the essence of this document, i.e., a critical summary of what was discussed in chapters 2-4 and what to expect in the future. It provides a concise link between all ideas discussed herein, aiming to provide to the reader the big picture of the investigation carried out and the real meaning of the contributions proposed in this thesis.

Finally, in Chapter 6 concluding remarks of this work are presented and in Chapter 7 all references used in this document are listed.

A literature review regarding each problem investigated is provided within the corresponding chapter.

2. INTENSIFICATION OF PHOTOCATALYTIC PROCESSES IN MICROFLUIDIC REACTOR USING TiO_2 AND TiO_2-GRAPHENE

This chapter is based on the paper entitled "Intensification of Photocatalytic Pollutant Abatement in Microchannel Reactor Using TiO_2 and TiO_2-Graphene" (*AIChE Journal*, Volume 62, Number 8, August 2016, Pages 2794–2802), by Natan Padoin, Luísa Andrade, Joana Ângelo, Adélio Mendes, Regina de Fátima Peralta Muniz Moreira and Cíntia Soares. Abstract, keyworkds, acknowledgements and references were omitted. It should be noticed that some minor amendments were performed in the text presented herein, but the procedures, results and conclusions reported in the original paper were not essentially affected.

2.1 INTRODUCTION

Recently, the application of microchannel technology has attracted great attention due to its potential for the intensification of chemical processes. Microchannel-based devices have been studied in heat and mass transfer operations, such as distillation, absorption and extraction (LAM, SORENSEN and GAVRIILIDIS, 2013; KENIG *et al.*, 2013), as well as in chemical reaction engineering (MILLS, QUIRAM and RYLEY, 2007). According to Gavriilidis *et al.* (2002), Jähnisch *et al.* (2004), Aran *et al.* (2011), Hartman, McMullen and Jensen (2011) and Nöel *et al.* (2015), microreactors are advantageous when compared to reaction vessels with conventional dimensions mainly due to the high surface-to-volume ratio, which leads to high heat and mass transfer. Chemical reaction rates are also favoured, particularly in heterogeneous reactions in which there is generally the deposition of a catalyst film on the inner walls of the device.

Microstructured reactors have a high surface-to-volume ratio (SU *et al.*, 2014; SU *et al.*, 2015; SU, HESSEL and NÖEL, 2015). Values in the order of 1×10^4 - 5×10^4 $m^2\cdot m^{-3}$ can be encountered, while in conventional reactors this ratio varies in the order of 10^2 - 10^3 (in rare cases) $m^2\cdot m^{-3}$ (JÄHNISCH *et al.*, 2004). Moreover, when heat transfer is involved, coefficients in the order of 10 $kW\cdot m^{-2}\cdot K^{-1}$ are encountered in microchannels (a value significantly superior to those obtained in traditional equipment), since this parameter is inversely proportional to the channel diameter (JÄHNISCH *et al.*, 2004). Thus, it is possible to rapidly remove or insert heat in a way that the chemical reactions may be conducted in perfect isothermal conditions and with precisely defined

residence times, which consequently enhances the selectivity, yield and quality of the products (JÄHNISCH *et al.*, 2004).

Although the chemical reaction kinetics is independent of the scale in which the process is carried out, the transport phenomena are not, opening the opportunity for process optimization in microstructured devices (GAVRIILIDIS *et al.*, 2002). According to Hartman, McMullen and Jensen (2011), the performance of mass transfer limited reactions is improved by two orders of magnitude in microreactors. Furthermore, microfluidic devices allow precise process control, require small space and generate low quantity of waste. Matsushita *et al.* (2008) also pointed out that microreactors exhibit short molecular diffusion path, fast mixing and are usually operated under laminar flow conditions.

When applied to photocatalytic processes, microreactors are advantageous due to the short irradiation path, which reduces the photon transport resistance (NÖEL, SU and HESSEL, 2015), commonly encountered in processes carried out in conventional reactors with catalyst immobilized on the inner walls (ARAN *et al.*, 2011), and allow spatial homogeneity of irradiance (SU *et al.*, 2014; SU *et al.*, 2015; SU, HESSEL and NÖEL, 2015; MATSUSHITA *et al.*, 2008). In fact, extensive research has been reported on the application of microchannel reactors in photocatalytic processes (SU *et al.*, 2015; SU, HESSEL and NÖEL, 2015; MATSUSHITA *et al.*, 2008; GORGES, MEYER and KREISEL, 2004; VAN GERVEN *et al.*, 2007; COYLE and OELGEMOLLER, 2008).

Few contributions are concerned about the use of this technology for the mitigation of environmental problems (CHARLES *et al.*, 2011; DEAN *et al.*, 2011; CHARLES *et al.*, 2012; CORBEL *et al.*, 2014; ZHANG *et al.*, 2009; OFFEMAN and HUMMERS, 1958). Furthermore, the effect of the operational conditions and geometry of the microchannels were not yet completely elucidated. It has been reported that the degradation of organic compounds depends on the dimensions of the microchannel (SU *et al.*, 2015) and the profiles of velocity and concentration of the pollutant (CHARLES *et al.*, 2011; CHARLES *et al.*, 2012). In some instances, mass transfer limitations on the overall rate of pollutant degradation are observed (ZHANG *et al.*, 2010). Additionally, even low cost materials can be used (RAMOS *et al.*, 2014) for photodegradation of a variety of compounds, such as indigo carmine, diclofenac and benzoylecgonine (REIS and LI PUMA, 2015), and photoinactivation of virus (REIS and LI PUMA, 2015). When compared with traditional batch vessels, microstructured reactors can reach reaction rates one order of magnitude higher (RAMOS *et al.* 2014).

Deep investigation about the fluid dynamics and the transport phenomena (especially mass transfer) are needed for enhanced design of photomicroreactors and for the application of this technology in large scale operations (SU *et al.*, 2014). According to Su *et al.* (2014), fundamental modeling aspects like the radiation distribution in microchannels, an essential parameter for integrating light source and reactor designs for process optimization, have not been published so far and are, thus, worthy of studying. Once rigorous models are available, the performance of photochemical microfluidic devices can be assessed and enhanced and challenging scale out strategies, such as the internal numbering up (SU *et al.*, 2014), can be better explored.

In this work, a microfluidic device was investigated aiming its application for photocatalytic processes. Titanium dioxide nanoparticles (TiO_2–Aeroxide® P25 from Evonik®) and a synthesized graphene-titanium dioxide composite catalyst (TiO_2-GR) were immobilized on the inner walls of a borosilicate glass microfluidic chip (Micronit® Microfluidics BV) using a layer-by-layer method. The effect of the operational conditions on the decolourization rate of methylene blue (model reagent) was also investigated. Finally, a rigorous computational model of the photocatalytic process, taking into account light distribution within the device, was implemented and validated by experimental data. This work distinguishes from the published literature in the area of photocatalytic pollutant abatement in microreactors by the investigation of the possibility of using a composite photocatalyst washcoat, which can be further optimized for sunlight harvesting, and the comprehensive computational modeling of the process herein studied, through coupled radiation distribution within the catalyst film and reactive flow based on fundamental physics of semiconductors.

2.2 MATERIALS AND METHODS

2.2.1 Microfluidic chip, catalysts and immobilization procedure

Commercial TiO_2 (Aeroxide® P25 from Evonik®) and a composite catalyst made of TiO_2 (P25) and graphene (1%) were immobilized on the inner walls of two distinct microfluidic chips (Micronit® Microfluidics BV, Enschede, The Netherlands, model R150.676). These chips are assembled with borosilicate glass through powder blasting technique and have an average total volume of 13 μL, a

surface/volume ratio of ~3.5×10^4 $m^2 \cdot m^{-3}$ and hydraulic diameter of ~133.5 μm (~0.78 m long).

The layer-by-layer immobilization of the TiO_2-P25 nanoparticles on the inner walls of the microfluidic chip was performed by passing a 1 $g \cdot L^{-1}$ aqueous suspension at pH equal to the point of zero charge of TiO_2-P25 (~7.5) intercalated with thermal treatments. The aqueous suspension was vigorously mixed, collected with a micropipette and injected in a port of the microdevice until it filled the channel. After removing the excess solution, the microfluidic chip was placed in a blow dryer (Hotwind System, Leister®, Switzerland) and submitted to thermal treatment (~25 ºC to 450 ºC in ~4 min, 450 °C for 5 min and 450 °C to ~30 ºC in 7 min). At the end of the thermal cycle, the microdevice was removed from the heating equipment and allowed to equilibrate with the room temperature. This procedure was repeated cyclically. Between cycles the microchip was submitted to optical analysis in a UV-VIS-NIR spectrophotometer (UV-3600, Shimadzu®, Japan). The transmittance (T) was obtained in the wavelength range of λ = 200-800 nm.

The TiO_2-graphene composite catalyst was synthesized using the hydrothermal method proposed by Zhang and co-workers (ZHANG *et al.*, 2010). Graphene oxide (GO) was prepared from graphene nano-platelets by oxidation with $KMnO_4$ in sulfuric acid – modified Hummer's method (HUMMERS and OFFEMAN, 1958). The detailed description of the composite preparation is given elsewhere (MAGALHÃES *et al.*, 2015).

A similar approach used for immobilization of the titanium dioxide nanoparticles (P25) was applied for supporting the composite P25-graphene photocatalyst on the inner walls of the microreactor. A 1 $g \cdot L^{-1}$ dispersion of the compound was prepared using distilled water and then sonicated for 30 min. The solution was then collected with a micropipette and injected in a port of the microdevice until it filled the channel. The device was then submitted to the thermal treatment previously described. However, in this case the thermal ramp consisted in heating from room temperature to 150 ºC, which was held for 30 min allowing for complete solvent evaporation. The device was then removed from the heating equipment and allowed to equilibrate with the room temperature. Among the immobilization cycles of TiO_2-GR, optical analysis were performed in the same manner previously described.

It should be noticed that all the procedure described above was carried out at the Faculty of Engineering of the University of Porto (FEUP), Portugal.

SEM images (JEOL® JSM-6390LV) were acquired from a microchannel containing TiO_2 nanoparticles before the conduction of chemical reactions (with accelerating voltage of 10 kV and magnifications of 65x and 500x). This procedure was conducted at Federal University of Santa Catarina (UFSC), Brazil.

2.2.2 Kinetics of methylene blue decolourization

The performance of the microfluidic device to degrade methylene blue dye ($C_{16}H_{18}ClN_3S \cdot 3H_2O$) was evaluated, since photocatalytic decolourization has been extensively studied in several reactor configurations (LING, MOHAMED and BHATIA, 2004; WU and CHERN, 2006; McCULLAGH *et al.*, 2010). A stock solution of methylene blue (Sigma®) was used to prepare aqueous solutions with concentrations of 1 $mg \cdot L^{-1}$ and 10 $mg \cdot L^{-1}$.

To allow fluid flow through the microchannels, 1/32" bonded-port Ultem® connectors from Labsmith® (Livermore CA, USA), supplied by Mengel Engineering (Virum, Denmark), were carefully glued on each port of the microreactor. One-piece PEEK fittings allowed leak-free interface between the port connectors to 1/32" OD, 250 μm ID PEEK tubing. A PEEK one-piece plug was attached to one of the port connectors allowing for a single-inlet/single-outlet setup.

The PEEK tubing was connected to flexible tubing (PharMed® BPT NSF-51) attached to a peristaltic pump (Ismatec®, IDEX® Health & Science GmbH, Germany) to control the continuous fluid flow from the methylene blue solution reservoir through the microfluidic chip. In particular, a mean residence time of τ = 8.6 s was adopted in the experiments. At the other side of the microreactor PEEK tubing was used to collect samples in glass vials, which were submitted to further spectroscopic analysis (UV-VIS-NIR spectrophotometer UV-3600, Shimadzu®, Japan) at the range of λ = 400-800 nm. The concentration of methylene blue at the end of the system was evaluated by spectrophotometric method at λ = 665 nm.

UV-A lamps (highest emission at λ = 365 nm, two 6 W black-light-blue bulbs, model VL-206-BL, Vilbert Lourmat, France) were used as photon source for the kinetics experiments, positioned at a distance of 15 cm above the microreactor. Light irradiance was measured at the surface of the microchip by radiometry (UV radiometer HD 2102.2, Delta/OHM, Italy) and the value of 6 $W \cdot m^{-2}$ was encountered. Minimum light dispersion in the experimental assays was ensured. Moreover, stray

light incidence on the experimental setup was blocked involving it with a black barrier.

Initially, the methylene blue solution was allowed to flow through the microchannel under dark conditions for the investigation of adsorption effect of dye molecules on the photocatalyst surface during the process. The solution was pumped through the device for 50 min. Thereafter, two samples were continuously collected in intervals of 40 min. This time interval was adopted for all sample collections since it yielded the volume required for the spectrophotometric analysis.

Based on the procedure adopted, all kinetic runs were carried out as follows: i) the methylene blue solution was pumped through the microreactor for 50 min under dark conditions; ii) then, an initial sample was collected for 40 min also under dark conditions; iii) the light was turned on; iv) samples were collected in time intervals of 40 min; and v) all samples were analyzed by spectrophotometry (absorbance measured at the wavelength of λ = 665 nm).

Additionally, an investigation of the influence of photolysis on the process was carried out. For that, the procedure above described was applied to a microfluidic chip with the same characteristics previously mentioned, but without any catalyst immobilized on its inner walls. The initial (under dark) and probe (under light) solutions were also analyzed in spectrophotometer at the wavelength of 665 nm. Figure 2.1 illustrates a scheme of the system adopted in the kinetic studies.

Figure 2.1: Experimental setup: (a) microfluidic chip at real scale; (b) sketch of the apparatus used for the investigation of methylene blue degradation kinetics.

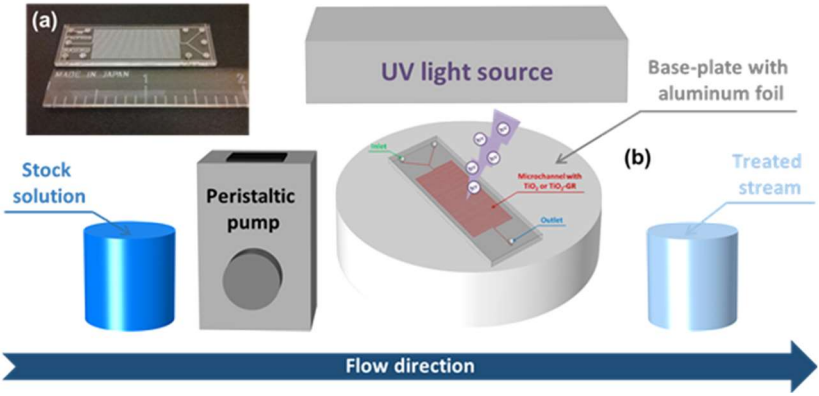

It should be noticed that all the procedure described above was carried out at the Faculty of Engineering of the University of Porto (FEUP), Portugal.

2.2.3 Computational modeling

Numerical simulations were conducted with the CAE tool COMSOL® Multiphysics (COMSOL Inc., Burlington, MA), version 4.3a. In particular, conditions similar to the experiments (C_0 = 1 mg·L^{-1} and τ = 8.6 s) were evaluated. Accordingly, a 3D model reproducing all features of the microfluidic chip used in the experiments was developed. The solution was supplied at one of the inlet ports with uniform velocity (u = 0.108 m·s^{-1}). At the extreme opposite of the channel null gauge pressure was assigned (p = 0 Pa). All other faces were impermeable to fluid flow and no-slip boundary condition was applied. The velocity and pressure fields inside the device was solved through Navier-Stokes equations (Eq. 2.1), coupled with the mass conservation equation (Eq. 2.2):

$$\rho(\mathbf{u}\cdot\nabla)\mathbf{u} = \nabla\cdot\left[-p\mathbf{I} + \mu\left(\nabla\mathbf{u} + (\nabla\mathbf{u})^{T'}\right)\right] + \mathbf{F} \tag{2.1}$$

$$\rho\nabla\cdot\mathbf{u} = 0, \tag{2.2}$$

where ρ (kg·m^{-3}) is the density, u (m·s^{-1}) is the velocity, t (s) is time, p (Pa) is the pressure, I (dimensionless) is the identity matrix, μ (kg·m^{-1}·s^{-1}) is the dynamic viscosity, T' is the transpose operator and F (N·m^{-3}) represent generic body forces. Steady-state, laminar and incompressible fluid conditions were assumed. It should be highlighted that creeping flow conditions (i.e., neglecting the inertial term in Eq. 2.1) could be used without significant impact on the final result.

Moreover, the reactive transport of methylene blue molecules within the microchannel was modeled through the convection-diffusion equation expressed by Eq. 2.3:

$$\nabla\cdot(-D_i\nabla C_i) + \mathbf{u}\cdot\nabla C_i = R_i, \tag{2.3}$$

where D_i (m^2·s^{-1}) is the species diffusion coefficient, C_i (mol·m^{-3}) is the species concentration and R_i (mol·m^{-3}·s^{-1}) is the species reaction rate. It is interesting to notice that the species transport model is coupled with the fluid flow model through the velocity field (***u***). In particular, the

photocatalytic reaction rate was modeled as a boundary condition at the microchannel walls (i.e., the volumetric reaction rate R_i was neglected), expressed through the rate presented in Eq. 2.4 (Nielsen *et al*., 2012):

$$-r = k_i C_i \left(\frac{\alpha I_0}{B p_0 n_0 \hbar\omega} \right)^{\gamma} \exp\left(-\gamma \alpha y\right), \tag{2.4}$$

where k_i is the pre-exponential factor (s^{-1}), C_i ($mol \cdot m^{-3}$) is the species concentration, α (m^{-1}) is the optical absorption coefficient, I_0 ($W \cdot m^{-2}$) is the incident UV irradiance, the term Bp_0n_0 ($\cong 3.3\times10^{-23}$ $m^3 \cdot s^{-1}$) represents the e^-/h^+ equilibrium, $\hbar\omega$ is the photon energy (5.44×10^{-19} J for UV at 365 nm), γ (dimensionless) is the electron transfer coefficient and y (m) are Cartesian coordinates.

According to Visan *et al.* (2014) the parameter γ can be considered equal to the unity for incident irradiance lower than $I_0 = 250$ $W \cdot m^{-2}$. Since the value of I_0 in the experiments was much lower than this limit ($I_0 = 6$ $W \cdot m^{-2}$), $\gamma = 1$ was considered in the computational modeling. The optical absorption coefficient α was taken as 6.264×10^5 m^{-1} (CHEN, LI and RAY, 2001). Finally, the pre-exponential factor k_i should be determined. Visan *et al.* (2014) obtained the intrinsic kinetic constant $k = 40$ s^{-1} for photocatalytic methylene blue degradation under UV irradiation at 365 nm with $I_0 = 180$ $W \cdot m^{-2}$. The authors found that in this condition the methylene blue degradation rate was approximately independent of the light intensity supplied to the system. Therefore, one can obtain the kinetic constant considering dependence on light intensity equating an apparent first order kinetic model to the generic expression derived by Nielsen *et al.* (2012). Through this procedure the light dependent apparent first-order kinetic constant was determined according to Eq. 2.5:

$$k_i \left(\frac{\alpha}{B p_0 n_0 \hbar\omega} \right)^{\gamma} = k_{app,LD} = 0.222\, s^{-1} \tag{2.5}$$

Since the value of the photocatalyst film thickness determined experimentally is lower than the cutoff criterion defined by Visan *et al.* (2014), a light independent model can be assumed, i.e., there is no necessity to evaluate the light intensity point by point inside the immobilized film and a logarithmic average can be considered, according to Eq. 2.6:

$$I_{avg} = \frac{I_0 - I_0 \exp(-\alpha\delta)}{\ln\left(\frac{I_0}{I_0 \exp(-\alpha\delta)}\right)} \tag{2.6}$$

Furthermore, the effect of internal mass transfer resistance within the photocatalyst film was accounted through the effectiveness factor (η), defined by Eq. 2.7:

$$\eta = \frac{\tanh \phi}{\phi}, \tag{2.7}$$

where ϕ is the Thiele modulus (dimensionless), expressed for a light dependent first-order reaction as:

$$\phi = \delta \sqrt{\frac{k_{app,LD} I_0^{\gamma}}{D_{eff}}}, \tag{2.8}$$

where δ is the film thickness (m) and D_{eff} ($m^2 \cdot s^{-1}$) is the effective diffusion coefficient, taken as $D_{eff} = D\varepsilon/\tau'$. The diffusion coefficient assumed the value $D = 4.1 \times 10^{-10}$ $m^2 \cdot s^{-1}$ (MILOZIC *et al.*, 2014), while the film porosity was defined as $\varepsilon = 0.45$ (VISAN *et al.*, 2014) and the tortuosity as $\tau' = 3.0$ (OULD-MAME, ZAHRAA and BOUCHY, 2000).

Therefore, converting the light dependent volumetric apparent first-order constant ($k_{app,LD}$) to a superficial constant, yielding $k''_{app,LD} = 6.25 \times 10^{-6}$ $m \cdot s^{-1}$, the superficial reaction rate applied to the computational model as a boundary condition was expressed according to Eq. 2.9:

$$-r'' = \eta k''_{app,LD} I_0^{\gamma} C_i \tag{2.9}$$

Complementary simulations in a 2D domain that represents the cross-section of the microchannel accounting the average film thickness was carried out to determine the average light intensity that effectively contributes to the photocatalytic reaction rate in the top, side and bottom layers of the device.

Firstly, the light absorption due to the glass layer positioned on the microchannel was accounted. Thus, considering that ~60% of the light

intensity is attenuated due to the glass contribution (determined by optical analysis in a microchip without any photocatalyst deposited on the inner walls, according to the procedure described previously, see Figure 2.2) and taking into account that the incident irradiance on the microfluidic chip surface was I_0 = 6.0 W·m^{-2}, one can notice that the effective light intensity that reaches the top photocatalyst layer was I_0^{eff} = 3.6 W·m^{-2}. The Beer-Lambert law (Eq. 2.10) was then applied to calculate the light propagation through the photocatalyst film layers (SU *et al*., 2014; VISAN *et al*., 2014; BOIYJOO, ANG and PAREEK, 2013).

$$\frac{dI}{dy} = -\alpha I \tag{2.10}$$

Different average intensities were obtained for the top, side and bottom photocatalyst layers. Therefore, the reaction rate was applied differently to each portion of the microchannel taking into account the respective average light intensity.

2.3 RESULTS AND DISCUSSION

2.3.1 Immobilization of the photocatalysts

Fig. 2.2a presents the optical profiles obtained during the immobilization procedure for the TiO_2 photocatalyst on the inner walls of the microreactor. The initial curve corresponds to the background profiles obtained from the microfluidic chip as acquired (i.e., without any treatment or fluid pumping). The curves tended to a stagnation profile. Specifically for the case of TiO_2 nanoparticles (P25), 16 cycles of immobilization on the microreactor walls were found to be needed for reaching this condition.

Notably, the sharpest variations in the optical profiles were observed in the range λ = 300-400 nm, corresponding to the region where TiO_2 harvests light. These observations are in line with the profiles obtained elsewhere (KIM *et al.*, 2013). Similarly, Fig. 2.2b presents the optical profiles obtained during the immobilization procedure for the composite photocatalyst of titanium dioxide and 1% of graphene (TiO_2-GR). Again, a variation mainly in the range λ = 300-400 nm was observed for transmittance profiles. The curves tended to a stagnation profile after only 8 immobilization cycles. This difference in the number of cycles

observed for P25 and its composite may be mainly due to the thickness of photocatalyst film deposited in each layer.

Figure 2.2: Transmittance profile evolution for (a) the microfluidic chip containing titanium dioxide nanoparticles (TiO_2-P25) and (b) composite catalyst of titanium dioxide and graphene (TiO_2-GR) immobilized on its inner walls.

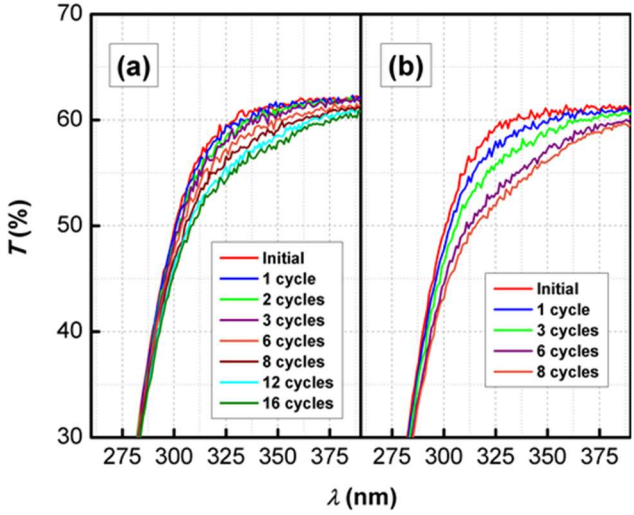

The Beer-Lambert law [$I = I_0 \cdot \exp(-\alpha \cdot \delta)$] allowed the estimation of the film thickness in both cases (TiO_2 and TiO_2-GR). Considering the absorption coefficient of TiO_2 as $\alpha = 6.264 \times 10^5$ m^{-1} at $\lambda = 365$ nm (CHEN, LI and RAY, 2001) the thickness of the TiO_2 and TiO_2-GR immobilized films was estimated as $\delta = 1.52$ µm. It should be highlighted, though, that the film thickness may vary along the channel length (i.e., the value found corresponds to an average). The absorption coefficient of TiO_2-GR was assumed equal to α for TiO_2 since graphene is nearly transparent to UV light.

The immobilization procedure adopted in this work, similar to that followed by Choi *et al.* (2001), represents a different criterion in comparison with the techniques commonly used in related studies in the literature, which generally adopted the mass variation of the microreactor between successive cycles to assess the progress of the deposition (CHARLES *et al.*, 2011; CORBEL *et al.*, 2014). In these works, a surface mass density was defined as cut off criterion: when this parameter reached a specified value, the deposition process was stopped. This procedure was

tested in the present work but without success, since there was no significant mass variation between successive cycles, even when evaluating it in a four decimal cases analytical balance.

Fig. 2.3 presents SEM images of cross-sections of the microchannel reactor containing TiO_2 nanoparticles immobilized on its inner walls, obtained at the center of the device.

Figure 2.3: SEM images of a cross section of the microreactor obtained at the center of the device. Magnification is highlighted in the respective pictures.

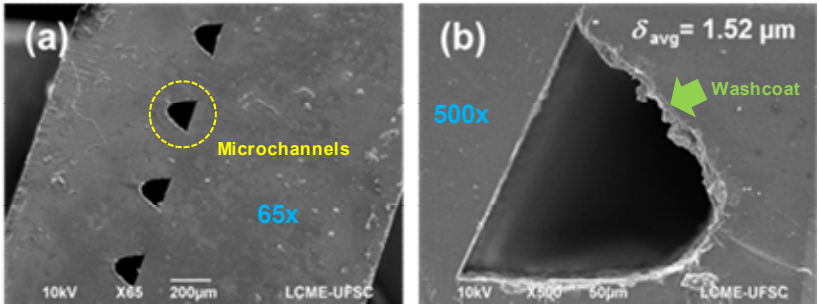

2.3.2 Methylene blue decolourization kinetics

Under dark conditions, the equilibrium of the adsorption of methylene blue (~0.0272 $g \cdot m^{-3} \cdot s^{-1}$) was achieved after 50 min, as evidenced in Fig. 2.4. The absorption spectra of the samples collected within the intervals of 50-90 min and 90-130 min under dark conditions were similar. Moreover, photolysis had a negligible effect on the process, as evidenced in Fig. 2.5.

Based on these preliminary observations, kinetic runs were carried out to assess the decolourization profiles of methylene blue in the microfluidic chip, aiming to determine the reaction rate. Fig. 2.6a presents the decolourization profiles obtained from the kinetic experiments using the microreactor containing titanium dioxide nanoparticles (P25) immobilized on its inner walls, while Fig. 2.6b shows the decolourization of methylene blue in the microreactor with TiO_2-GR immobilized on the walls.

Figure 2.4: Absorption spectrum of the methylene blue dye in the preliminary study under dark conditions.

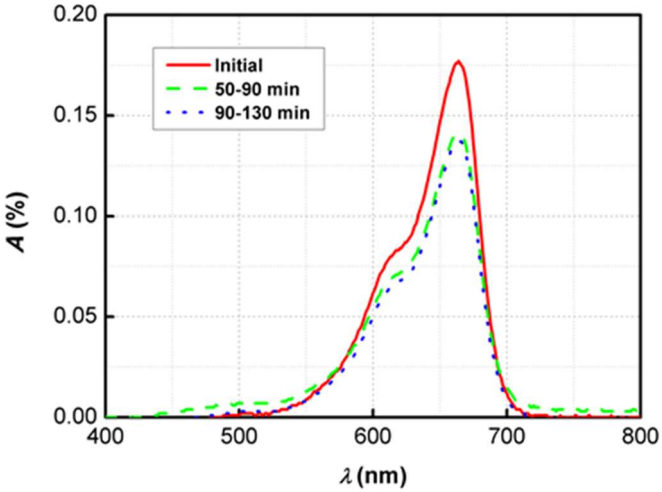

Figure 2.5: Absorption spectrum of the methylene blue dye in the preliminary study of photolysis effect on the performance of the system.

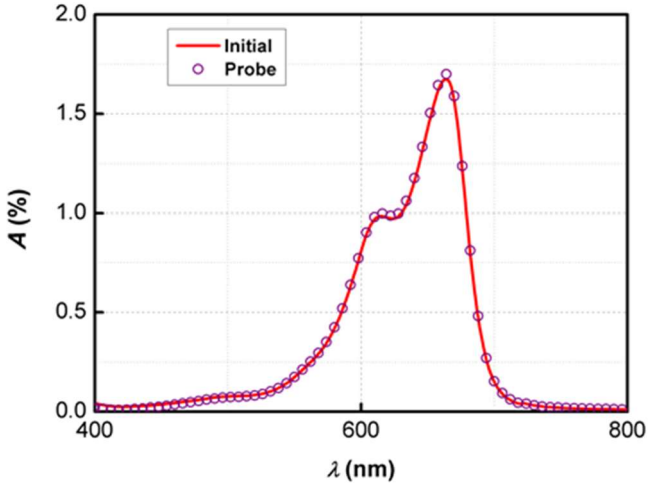

It is possible to observe that a steady-state condition was reached for all cases. A lower initial concentration led to a more pronounced decolourization percentage (i.e., lower values of C/C_0). For τ = 8.6 s and C_0 = 10 mg·L^{-1} the equilibrium was reached at C/C_0 = ~0.85 (i.e., ca. 15% of decolourization was observed). On the other hand, for the same value of τ and considering C_0 = 1 mg·L^{-1} the steady-state decolourization ratio was C/C_0 = ~0.30 (i.e., ca. 70% of decolourization). Similarly, Fig. 2.6b presents the decolourization profiles for the microreactor containing composite catalyst of titanium dioxide and graphene (TiO_2-GR) immobilized on its inner walls. For τ = 8.6 s and C_0 = 10 mg·L^{-1} the equilibrium was reached at C/C_0 = ~0.80 (ca. 20% of decolourization). For C_0 = 1 mg·L^{-1} the steady-state decolourization ratio was C/C_0 = ~0.20 (i.e., ca. 80% of decolourization).

Figure 2.6: Decolourization profiles of methylene blue obtained with (a) the microfluidic chip containing titanium dioxide nanoparticles (TiO_2 P25) immobilized on its inner walls and (b) the microfluidic chip containing composite catalyst of titanium dioxide and graphene (TiO_2-GR) immobilized on its inner walls. The subindex *n* represents the samples acquired.

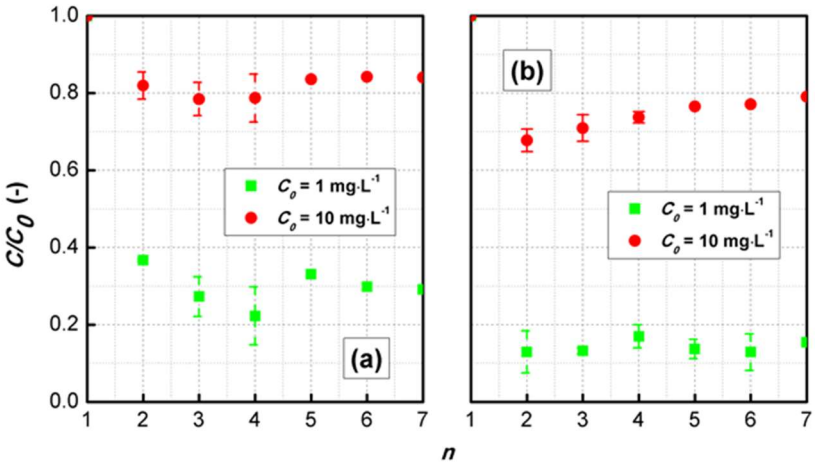

Clearly, it is possible to observe that a higher initial decolourization percentage was observed for the microfluidic chip containing composite catalyst of titanium dioxide and graphene (TiO_2-GR) immobilized on its inner walls. However, the equilibrium values obtained at the steady-state for both devices were similar. Thus, it is

possible to point out that graphene is influencing the effectivity of the chemical reaction, especially at the early stage. Since the work of Willians, Seger and Kamar (2008) there is an increasing interest in the use of graphene-based composite semiconductors for photocatalysitc processes due to their outstanding properties. According to previous findings (MAGALHÃES *et al.*, 2015), the enhanced activity of TiO_2-GR may be attributed to the decrease in e^-/h^+ recombination, since graphene has the ability to accept the electrons photogenerated by P25, as well as the increased adsorption of methylene blue on the graphene sheets. These observations are in line with other works published elsewhere (ZHANG *et al*., 2010; NGUYEN-PHAN *et al.*, 2011). In fact, the adsorption capacity of graphene sheets is about fourfold higher than pure P25 and twofold higher than P25-GR (MAGALHÃES *et al.,* 2015). Nguyen-Phan *et al.* (2011) reported the photodegradation of methylene blue by TiO_2-GR composite photocatalysts and also found enhanced performance of this composite when compared to pure TiO_2 nanoparticles. Moreover, Wu *et al.* (2015) reported enhanced photocatalytic activity when evaluating the decolourization of methylene blue solutions treated with TiO_2 nanocrystals supported on graphene-like bamboo charcoal.

Based on this scenario, the enhanced initial reaction rate of the photocatalytic film of composite TiO_2-GR can be explained as follows: due to the high surface area of graphene sheets, the adsorption rate of methylene blue molecules on the surface of the photocatalyst is higher than the reaction rate until a saturation is reached, when the reaction rate equals the adsorption rate. From this point on, the reaction rate turns out to be higher than the adsorption rate and is approximately equal to the apparent reaction rate observed in pristine TiO_2 nanoparticles. Therefore, methylene blue decolourization proceeds with a rate similar to that achieved with P25, eventually leveling-off to the same equilibrium level obtained with the model photocatalyst. In other words, graphene altered the kinetics of methylene blue decolourization in the microfluidic chip but did not alter the thermodynamic state of the system.

2.3.3 Kinetics modeling

Assuming that the device can be modeled as a pseudo-PFR reactor, the experimental apparent reaction rate constant can be obtained according to Eq. 2.11 (VISAN *et al.*, 2014; STEFANOV *et al*., 2011):

$$u\frac{dC_i}{dx} = -k_{app}C_i, \tag{2.11}$$

where u ($m \cdot s^{-1}$) is the mean velocity at the microchannel (assumed constant), C_i is the concentration ($mg \cdot L^{-1}$), x (m) are the coordinates along the reactor length and k_{app} (s^{-1}) is the volumetric apparent first-order reaction rate constant.

For the microchannel containing TiO_2 immobilized on its inner walls operating at $\tau = 8.6$ s and $C_0 = 1$ $mg \cdot L^{-1}$, the apparent reaction rate constant *is* $k_{app} = 0.17$ s^{-1}. However, for $C_0 = 10$ $mg \cdot L^{-1}$ $k_{app} = 0.0226$ s^{-1}. Since there was not a linear variation of k_{app} when the inlet concentration was increased, the reaction probably follows a Langmuir-Hinshelwood-Hunge-Watson (LHHW) mechanism. Moreover, when the residence time was decreased to $\tau = 5.8$ s, the apparent reaction rate assumed the value $k_{app} = 0.14$ s^{-1} for $C_0 = 1$ $mg \cdot L^{-1}$ and $k_{app} = 0.038$ s^{-1} for $C_0 = 10$ $mg \cdot L^{-1}$.

Applying the same procedure to the TiO_2-GR catalyzed reactions, k_{app} assumed the values 0.22 s^{-1} and 0.031 s^{-1} for $C_0 = 1$ $mg \cdot L^{-1}$ and $C_0 = 10$ $mg \cdot L^{-1}$, maintaining the mean residence time fixed in $\tau = 8.6$ s.

Therefore, in the microfluidic chip with TiO_2 immobilized on the inner walls submitted to $C_0 = 10$ $mg \cdot L^{-1}$ and $\tau = 8.6$ s, the decolourization rate of methylene blue was $-r_A = \sim 0.209$ $g \cdot m^{-3} \cdot s^{-1}$ at the steady state. In addition, a reaction rate of $-r_A = \sim 0.0988$ $g \cdot m^{-3} \cdot s^{-1}$ was observed at the steady state when carrying out the reaction with $C_0 = 1$ $mg \cdot L^{-1}$ and residence time of 8.6 s. When the reaction was conducted at $C_0 = 10$ $mg \cdot L^{-1}$ and the residence time was reduced to 5.8 s, a decolourization rate of $-r_A = \sim 0.35$ $g \cdot m^{-3} \cdot s^{-1}$ was observed.

In the microreactor containing TiO_2-GR immobilized on its inner walls submitted to $C_0 = 10$ $mg \cdot L^{-1}$ and $\tau = 8.6$ s, the decolourization rate of methylene blue was $-r_A = \sim 0.278$ $g \cdot m^{-3} \cdot s^{-1}$ at the steady state. Additionally, a decolourization rate of $-r_A = \sim 0.109$ $g \cdot m^{-3} \cdot s^{-1}$ was obtained for $C_0 = 1$ $mg \cdot L^{-1}$ and residence time of 8.6 s at the steady state. Table 1 presents a summary of the reaction rates observed (for TiO_2 and TiO_2-GR).

Table 2.1: Summary of the experimental conditions adopted in this study and the respective reaction rates observed.

Photocatalyst	$C_{0,MB}$ (mg·L^{-1})	τ (s)	I_0 (W·m^{-2})	$-r_A$ (g·m^{-3}·s^{-1})
TiO_2	1	8.6	6	0.0988
	10			0.209
		5.8		0.35
TiO_2-GR	1	8.6		0.109
	10			0.278

Therefore, there was no significant difference between the microreactors containing TiO_2 and TiO_2-GR immobilized on their inner walls in terms of reaction rates at the steady state. However, a higher initial reaction rate was observed in the microreactor containing TiO_2-GR, particularly for C_0 = 10 mg·L^{-1}. Additionally, it should be emphasized that the film of TiO_2 tended to be more stable compared to the reactor containing TiO_2-GR since in the former the photocatalyst was deposited at a high-temperature (450 °C) that allowed the sintering of the material on the walls of the microfluidic chip. This temperature could not be applied for the thermal annealing of the TiO_2-GR photocatalyst since it would certainly promote severe damage to the carbon structure of the graphene and, thus, modify its chemical identity. The temperature used for the thermal treatment of the microreactor containing TiO_2-GR (150 °C) probably did not promote a tight adhesion of the photocatalyst film on the walls of the microchannels, contributing to further deactivation due to the flow shear stress.

Furthermore, in the microreactor containing TiO_2, the steady state was reached after 80 min for C_0 = 10 mg·L^{-1} and 120 min for C_0 = 1 mg·L^{-1} after light was turned on. On the other hand, the steady state was obtained after 120 min for C_0 = 10 mg·L^{-1} and 80 min for C_0 = 1 mg·L^{-1} in the microreactor containing TiO_2-GR. Thus, there was a distinct behavior between the two systems studied in terms of time interval needed to reach the steady state. Interestingly, the opposite behavior was observed in terms of the initial methylene blue concentration.

Ling, Mohamed and Bhatia (2004) studied the photocatalytic decolourization of methylene blue in a tubular reactor (ID = 1.3 cm, L = 25 cm, 10 pieces) containing TiO_2 immobilized in its inner walls. When operating at the temperature of 30 °C, pH of 6.9, catalyst mass of 0.25 g, air bubbling of 2.5 cm^3·s^{-1} and initial methylene blue concentration of C_0 = 40 μM (~15 mg·L^{-1}) a reaction rate of $-r_A$ = 0.004 g·m^{-3}·s^{-1} was

achieved. Reaction rates ~50x and ~90x higher were observed in our experiments when operating the microreactor containing TiO_2 nanoparticles immobilized on the inner walls (C_0 = 10 mg·L^{-1}; τ = 8.6 s and τ = 5.8 s, respectively). Ling, Mohamed and Bhatia (2004) worked with an aerated medium, which naturally enhances the photocatalytic activity, a condition that was not used in our experiments. Therefore, the advantage of the use of microreactors for the intensification of photocatalytic reactions was demonstrated, since it can reach higher reaction rates compared to conventional equipment.

A maximum apparent first-order reaction constant of k_{app} = 0.17 s^{-1} was obtained when operating with C_0 = 1 mg·L^{-1} and τ = 8.6 s and TiO_2 immobilized on the reactor walls. When TiO_2-GR was considered, $k_{app,max}$ = 0.22 s^{-1} under the same operational conditions. These values are slightly lower than the apparent first-order reaction rate constant reported by Visan *et al.* (2014) (k_{app} = 0.3 s^{-1}). Moreover, the values of k_{app} obtained in this study are considerably lower than the intrinsic value (k = 40 s^{-1}) (VISAN *et al.,* 2014).

It should be highlighted that the model represented by Eq. 2.11 represents a strong simplification of the photochemical microflow investigated herein. First of all, a constant average velocity is used in this simplified model. It implies that plug flow is assumed. In addition, an average reaction rate and an average pseudo-first order reaction velocity constant are obtained from this simplified model. These averages arise from the integration of Eq. 2.11 along the reactor length. Therefore, the microfluidic device was treated as a differential reactor in this approximation. Given the conversions obtained, this assumption is not strictly valid. Therefore, the results obtained in this section should be viewed only as a rough estimate of the reactor performance considering such a strong approximation. Nevertheless, it should be noted that the results obtained from the simplified model expressed by Eq. 2.11 were not used, in any instance, in the computational modeling whose procedure was described in section 2.2.3 and results will be presented in the next section (2.3.4). This computational model does not consider any of the assumptions assumed for the use of Eq. 2.11 and consists in a rigorous description of the system, considering the fundamental physics of semiconductors as starting point and accounting for the coupling of radiation distribution, fluid flow, mass transport and chemical reactions, consisting in a robust and reliable model that comprehensively describes the reactive flow in the microfluidic device.

2.3.4 Computational modeling

Figure 2.7 presents the results obtained from the computational simulations according the workflow discussed previously. Particularly, Fig. 2.7a shows the light intensity distribution in a cross section of the channel considering the walls covered with a TiO_2 film with the same average thickness obtained experimentally.

It is possible to observe that considerably distinct average light intensities were obtained in each of the films layers. At the top of the microchannel, where the photocatalyst film was directly exposed to UV irradiation through a back-side illumination mechanism (CHEN, LI and RAY, 2001), the average light intensity was I_{avg} = 2.327 W·m^{-2}. On the other hand, at the side and bottom photocatalyst layers, subjected to a front-side illumination mechanism (CHEN, LI and RAY, 2001), the average light intensities were $I_{avg} = 4.273\times10^{-1}$ W·m^{-2} and $I_{avg} = 7.536\times10^{-1}$ W·m^{-2}, respectively.

Additionally, it should be stressed that the effect of internal mass transfer within all photocatalyst layers can be neglected, since the average effectiveness factor was close to the unity in all scenarios: $\eta = 9.987\times10^{-1}$, $\eta = 9.996\times10^{-1}$ and $\eta = 9.998\times10^{-1}$ for the top, side and bottom layers, respectively. These results indicate that the entire film was exposed to approximately the same reaction conditions obtained at the catalyst surface.

Figure 2.7b highlights the light intensity profile obtained through a line that crosses the channel cross section vertically at the center. One can notice that the higher light absorption occurs at the top layer of photocatalyst film, when I decreases from 3.6 W·m^{-2} to approximately 1.4 W·m^{-2}. In addition, light intensity was attenuated from ~1.4 W·m^{-2} to ~0.5 W·m^{-2} within the bottom layer.

Finally, a computational study was carried out in the 3D domain representing all features of the experimental setup, as described previously. Figure 2.7c presents the results obtained. In particular, it should be highlighted that the methylene blue degradation equilibrium obtained numerically was significantly close to the experimental result (~3% deviation was observed). Therefore, the computational model was validated and can be used for further investigations aiming to the scale-out of photocatalytic processes in microfluidic systems, following numbering-up strategies (SU et al., 2014) as reported elsewhere (SU et al., 2016; RUSSO et al., 2016).

Figure 2.7: Computational model of methylene blue degradation in the microchannel containing titanium dioxide nanoparticles (TiO_2-P25) immobilized on its inner walls: (a) light distribution at the photocatalyst layers (top, side and bottom); (b) light intensity profile in a vertical line crossing the center of the computational domain; (c) degradation profile obtained at the steady state (C_0 = 1 mg·L^{-1} and τ = 8.6 s) in the 3D geometry. Details about average light intensity, Thiele modulus and effectiveness factor at each film layer are also presented.

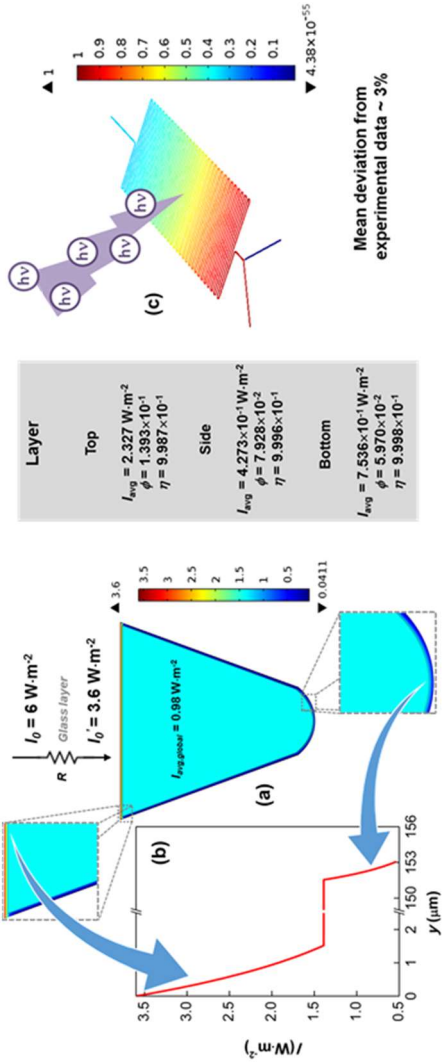

2.4 CONCLUSIONS

The feasibility of using microfluidics for photocatalytic applications in a 133.5 μm internal hydraulic diameter borosilicate glass commercial microfluidic chip was demonstrated. TiO_2 and composite catalyst of TiO_2 and graphene (TiO_2-GR) were used as photocatalysts and were deposited on the inner walls of the microchip using the optical profile evolution as a criterion. A kinetic study using methylene blue as model reagent was carried out for the evaluation of the system performance. Although TiO_2-GR allowed for a higher initial reaction rate, the decolourization level was similar for both photocatalysts at the steady state. The observed reaction rate was at least one order of magnitude higher than that observed in reactors with conventional dimensions reported in the literature. This evidenced the potential use of microfluidic systems for process intensification. Recognized features of microchannel-based devices such as high area/surface ratio, fast mixing and short diffusive and photonic path contributed to the observed behavior. Furthermore, a comprehensive computational model was implemented and validated by experimental data. This model will be used for further scale-out studies based on internal numbering-up strategies.

2.5 IMPRESSIONS AND PERSPECTIVES

Some difficulties were encountered during the development of the research reported in this chapter and are worth of discussion. Initially the photocatalyst deposition method consisted in pumping a suspension of the respective nanoparticles through the microchannels using a peristaltic pump followed by drying in a ventilated oven at 60 ºC, according to the procedure described elsewhere. Also, the progress of the deposition was evaluated by weighting the microfluidic chips in an analytical balance. This method was not suitable because drying in a ventilated oven required a long period (several hours) for each cycle and the resulting deposited film was clearly non-uniform (by visual inspection). Trying to measure the amount of deposited material by weighting the chip was also inadequate, since no variations in mass were observed even in a 5-digit analytical balance. Furthermore, it is worth to highlight that using a peristaltic pump to flow the nanoparticle suspension (only TiO_2 was tested up to this point) through the microchannel was also inappropriate. When the process was carried out at 60 ºC the material was not tightly deposited on the walls and a high shear resulted from the

pumping. Thus, at each cycle the material deposited from the previous step was almost entirely washed out.

In a tentative to improve this method a new (non-ventilated) oven was used, allowing high temperatures. Only TiO_2 was considered in the first tests and the goal was to carry out the cycles at 450 ºC to allow the sintering of the photocatalyst on the internal walls of the microfluidic chip, which would eliminate the problem of wash out due to the pumping of the suspension through the microchannel. However, this oven did not allow a controlled temperature ramp (the temperature oscillated significantly around the set point). Besides, even though it was possible to rapidly heat the system from ambient temperature to ~450 ºC, several hours were needed to cool the chamber until an acceptable temperature was reached allowing to withdraw the chip from the equipment. Moreover, a clearly non-uniform deposition was still obtained. Also, no variations in the total mass of the microfluidic chip were observed when weighting it in a 5-digit analytical balance.

These problems were only definitely solved when drastic changes were considered in the procedure adopted. Pumping the suspension of nanoparticles through the microchannel with a peristaltic pump was replaced by gently inserting the fluid from one of the ports of the device with a micropipette. In addition, the evaporation of the solvent (water) was performed in a blow dryer with precisely controlled heating ramp. It became possible to heat the microfluidic chip containing the suspension of nanoparticles from ambient temperature to ~450 ºC in ~5 min and cool the system from ~450 ºC to room temperature in ~7 min. Also, the temperature was maintained at the set point (450 ºC) along the entire process, which lasted for 5 min in each cycle for the deposition of TiO_2. Finally, the deposition evolution was monitored by a spectroscopic method, measuring the transmittance of light at a wavelength range of 200 – 800 nm. This measurement technique was significantly sensitive.

It should be highlighted that a virgin chip was used in each of these tests, to ensure replicability of the best scenario to be determined. Additionally, it is important to mention that the period of thermal treatment at 450 ºC for the case of deposition of TiO_2 (5 min) was determined by trial and error and corresponded to the minimal interval of time necessary to ensure a uniform deposition (by visual inspection). Again, a virgin chip was used in each of these trials.

Once the procedure for deposition of TiO_2 was optimized, tests were performed to deposit the composite photocatalyst (TiO_2-GR) in a similar way. Obviously, there was a temperature limitation, since performing the cycles of 450 ºC would remove the carbon from the

catalyst. Based on the previous experience of the group at LEPABE/FEUP (Portugal), where all experiments were carried out, a temperature limit of 150 ºC was specified for the deposition of TiO_2-GR. Several trials were performed, each one in a virgin chip, to determine the best time interval for the heat treatment that would ensure complete evaporation of the solvent and uniform deposition (by visual inspection). The best condition was heating the system at 150 ºC for 30 min in each cycle.

The method used in this study, although effective, led to an irregularly deposited film, as further observed in SEM images obtained at a transversal region of the microfluidic chip. Moreover, the stability of the film deposited was significantly different: while the microfluidic chip containing TiO_2 immobilized was able to maintain its catalytic activity for a long period (at least two years, taking as reference the time at which this document has been written), the chip containing TiO_2-GR lost its activity after few utilizations. Therefore, further research is needed aiming to investigate means of enhancing the stability of immobilized carbon-based composite photocatalyst. In addition, the use and/or development of methods able to produce a regular film deposited on the microchannel walls is desired.

Moreover, it should be considered that, as stated in Chapter 1, a composite photocatalyst of TiO_2 and graphene was used in this study, but any other composite material could also be tested. Therefore, further investigation should be carried out aiming to study methods of deposition of different composite photocatalysts and the performance of the systems obtained. This research is important to determine optimal conditions for photochemical microreactors able to harvest sunlight.

From the point of view of the computational modeling developed in this chapter, the main difficulty observed was the construction of a numerical mesh that could be computationally efficient in terms of memory usage for the case of the three-dimensional platform.

The computational model developed herein should be used to investigate the effect of different arranges of photocatalytic films on the internal walls of microfluidic devices aiming to determine the best global configuration. Moreover, this model could be applied to investigate the performance of photochemical microfluidic systems under different scenarios, including the development of strategies for the *scale out* of this technology.

3. AN EXPLICIT CORRELATION FOR OPTIMAL TiO_2 FILM THICKNESS IN IMMOBILIZED PHOTOCATALYTIC REACTION SYSTEMS

This chapter is based on the paper entitled "An Explicit Correlation for Optimal TiO_2 Film Thickness in Immobilized Photocatalytic Reaction Systems" (*Chemical Engineering Journal*, Volume 310, Part 2, 15 February 2017, Pages 381–388), by Natan Padoin and Cíntia Soares. Copyright © 2016 Elsevier B.V. Abstract, keywords, acknowledgements and references were omitted. It should be noticed that some minor amendments were performed in the text presented herein, but the procedures, results and conclusions reported in the original paper were not essentially affected.

3.1 INTRODUCTION

Photocatalysis is a photoelectrochemical process based on a semiconductor photocatalyst (usually TiO_2 in environmental applications). When the photocatalyst is irradiated with photons with adequate energy, electrons are excited to the conduction band, creating an electron/hole (e^-/h^+) pair. Holes generate hydroxyl ($OH^\bullet$) radicals from the water molecules adsorbed at the material surface, while the electrons can convert adsorbed oxygen to superoxide anion ($O_2^{\bullet-}$) (ÂNGELO *et al.*, 2013). These radicals have the ability to, respectively, oxidize and reduce chemical compounds usually adsorbed on the photocatalyst surface. Figure 3.1a presents an overview of this phenomenon.

Figure 3.1: Overview of the mechanism involved in photocatalytic processes (a). Photocatalytic film illuminated according to the (b) BSI and (c) FSI mechanisms.

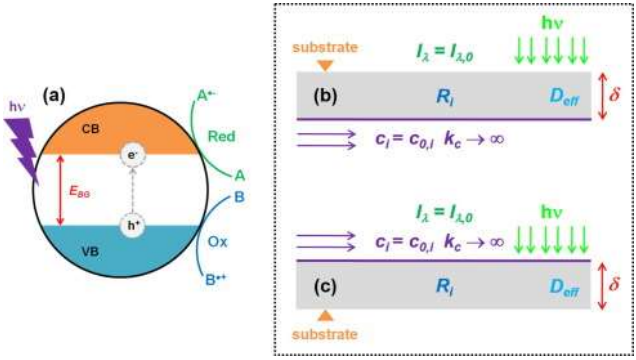

According to Boyjoo, Ang and Pareek (2013), photocatalytic reactors can be arranged in immobilized (i.e., with the photocatalyst attached to the active walls) or suspended (i.e., considering the photocatalyst dispersed in the fluid phase) forms. Suspended reactors offer enhanced mass transfer coefficients, while immobilized devices do not require post-treatment for recovery of the catalyst nanoparticles (BOYJOO, ANG and PAREEK, 2013). Moreover, in immobilized reactors light is used more efficiently when compared with the suspended arrange. However, the former configuration is only effective in devices with high surface-to-volume ratio, which can be achieved in microchannel reactors (SU *et al.*, 2014; SU *et al.*, 2015; SU, HESSEL and NOËL, 2015; GAVRIILIDIS *et al.*, 2002; JÄHNISCH *et al.*, 2004; ARAN *et al.*, 2011; HARTMAN, McMULLEN and JENSEN, 2011; NOËL, SU and HESSEL, 2015). When applied to photocatalytic processes, microreactors allow high mass transfer rates (HARTMAN, McMULLEN and JENSEN, 2011) and reduced photon transport resistance (NOËL, SU and HESSEL, 2015), with consequent homogeneity of irradiance (SU *et al.*, 2014; SU *et al.*, 2015; SU, HESSEL and NOËL, 2015; MATSUSHITA *et al*., 2008), leading to high reaction rates.

Due to these characteristics, microfluidic reactors have been successfully applied in photocatalyzed synthetic routes (SU *et al.*, 2015; SU, HESSEL and NOËL, 2015; MATSUSHITA *et al.*, 2008; GORGES, MEYER and KREISEL, 2004; VAN GERVEN *et al.*, 2007; COYLE and OELGEMOLLER, 2008) and for photocatalytic pollution control (CHARLES *et al.*, 2011; DEAN *et al.*, 2011; CHARLES *et al.*, 2012; CORBEL *et al.*, 2014; RAMOS *et al.*, 2014; REIS and LI PUMA, 2015).

However, for the maximization of the reacting system performance, a comprehensive investigation of the fluid dynamics, transport phenomena and radiation distribution within these devices is needed. In particular, the radiative transport in immobilized systems occur through two mechanisms: backside illumination (BSI) or front-side illumination (FSI) (CHEN, LI and RAY, 2001) (see Figure 3.1b,c).

In the BSI mechanism, the incident irradiation ($I_\lambda = I_{\lambda,0}$) and the fluid flow (with $c_i = c_{0,i}$) take place in opposite sides of the film (Figure 3.1b). On the other hand, in the FSI mechanism both phenomena occur at the same side of the photocatalytic film (Figure 3.1c). Therefore, different species concentration profiles are expected depending on the illumination arrange. In fact, the FSI mechanism can be compared to the co-current operation in traditional chemical processes, while the BSI scheme corresponds to the counter-current method.

In microfluidic reactors, frequently a combination of BSI and FSI mechanisms is encountered. Modeling the complex and coupled phenomena taking place within the film is, therefore, necessary for proper optimization of the reactive system. Nielsen *et al.* (2012) and Visan *et al.* (2014) proposed interesting models for the evaluation of the performance of microchannel reactors. The model developed by Visan *et al.* (2014) includes the liquid and solid phases in the formulation and is able to indicate which phase imposes higher resistance to the chemical reaction. On the other hand, Nielsen *et al.* (2012) provided a useful kinetic formulation based on the fundamental physics of semiconductors and developed a model concentrated at the solid phase. However, there are no models available in the literature that are able to explicitly predict the optimal photocatalytic film thickness in immobilized systems subjected to BSI and FSI arranges. Based on this scenario, in this work equations have been proposed for the prediction of the best TiO_2 film thickness for BSI and FSI arranges as a function of the incident irradiation ($I_{\lambda,0}$), the apparent first-order reaction constant ($k_{r,app}$), the effective diffusivity (D_{eff}) and the absorption coefficient (κ_λ).

3.2 METHOD

3.2.1 Governing equations and boundary conditions

3.2.1.1 Radiation modeling

According to Boyjoo, Ang and Pareek (2013), "the traveling of photonic rays with their corresponding energy loss due to absorption and out-scattering and energy gain due to in-scattering of photonic energy" can be described according to Eq. 3.1, known as Radiative Transport Equation (RTE):

$$\frac{dI_\lambda(s,\Omega)}{ds} = -\kappa_\lambda I_\lambda(s,\Omega) - \sigma_\lambda I_\lambda(s,\Omega) + \\ + \frac{1}{4\pi}\sigma_\lambda \int_0^{4\pi} p(\Omega' \to \Omega) I_\lambda(s,\Omega')\, d\Omega', \tag{3.1}$$

where the first, second and third terms of the right-hand side represent the absorption, out-scattering and gain of energy due to in-scattering of radiation, respectively (BOYJOO, ANG and PAREEK, 2013).

When immobilized systems are considered, the effect of light scattering may be neglected and only absorption of radiation occurs with the deposited film of photocatalyst (BOYJOO, ANG and PAREEK, 2013). In this case Eq. 3.1 may be simplified according to Beer-Lambert's law, resulting in Eq. 3.2 solved herein (BOYJOO, ANG and PAREEK, 2013; SU *et al.*, 2014; VISAN *et al*., 2014):

$$\frac{dI_{\lambda}(s)}{ds} = -\kappa_{\lambda} I_{\lambda}(s) \tag{3.2}$$

The Dirichlet boundary condition was prescribed at the film surface directly exposed to external photonic flux, according to Eq. 3.3:

$$I_{\lambda,s} = I_{\lambda,0} \tag{3.3}$$

At the remaining boundaries the normal derivative of the irradiance was set as zero. However, it should be highlighted that Eq. 3.2, as a boundary value problem, can be integrated to yield the algebraic expression represented by Eq. 3.4:

$$I_{\lambda}(s) = I_{\lambda,0} e^{-\kappa_{\lambda} s} \tag{3.4}$$

3.2.1.2 Species transport modeling

Species *i* transport within the photocatalytic film was modeled through Eq. 3.5, assuming steady state and neglecting convection in the porous domain:

$$\nabla \cdot \mathbf{N}_i = R_i \tag{3.5}$$

In particular, the diffusive flux ($\boldsymbol{N}_i$) was accounted based on Fick's first law, considering diluted species concentration, according to Eq. 3.6:

$$\mathbf{N}_i = -D_{eff} \nabla c_i \tag{3.6}$$

Since the photocatalytic film is a porous structure, an effective diffusion coefficient was taken into account through a correction of the

species diffusivity (D_i) with the porous medium intrinsic macroscopic properties (Eq. 3.7):

$$D_{eff} = \frac{D_i \varepsilon}{\tau} \tag{3.7}$$

Finally, the volumetric rate of disappearance of species *i* within the film was modeled through Eq. 3.8:

$$R_i = -\eta k_{r,app} c_i I_\lambda^{\gamma} \left(1-\varepsilon\right) \tag{3.8}$$

The apparent first-order reaction rate constant was taken from Visan *et al.* (2014) ($k_{r,app}$ = 0.222 s^{-1}) for methylene blue (used as a reference herein), considering in this development the kinetic model derived from fundamental physics of semiconductors proposed by Nielsen *et al.* (2012). The kinetic model was validated in a previous study of our group. It should be highlighted that the light dependent model (LDM), which takes into account the light intensity point-by-point in the rate equation (VISAN *et al.*, 2014), was considered in this work.

As noticed from Eq. 3.7, the reaction rate within the film was corrected through the effectiveness factor (η) (Eq. 3.9):

$$\eta = \frac{\tanh \phi}{\phi} \tag{3.9}$$

The effectiveness factor corrects the reaction rate inside the porous catalyst, subjected to mass transfer resistance, taking into account the species *i* concentration at the surface of the film as reference. Therefore, the effect of the porous matrix on the reactive species transport was considered in all simulations. In Eq. 3.9 the parameter ϕ refers to the Thiele modulus (ratio of reaction to diffusion velocity within the catalyst), defined according to Eq. 3.10:

$$\phi = \left(\delta - y\right) \sqrt{\frac{k_{r,app} I_{\lambda,0}{}^{\gamma}}{D_{eff}}} \tag{3.10}$$

In Eqs. 3.8 and 3.10 the coefficient γ assumed the value 1.0, as recommended by Visan *et al.* (2014). Moreover, D_{eff} was defined as

6.15×10^{-11} $m^2 \cdot s^{-1}$ (according to Eq. 3.7, where D_i = 4.1×10^{-10} $m^2 \cdot s^{-1}$ (MILOZIC *et al.*, 2014), ε = 0.45 (VISAN *et al.*, 2014) and τ = 3.0 (OULD-MAME, ZAHRAA and BOUCHY, 2000). At the film surface exposed to the fluid flow transporting species *i* a prescribed concentration boundary condition was applied, according to Eq. 3.11:

$$c_i = c_{0,i} \tag{3.11}$$

It should be highlighted that the resistance to species *i* transport in the fluid phase was neglected ($k_c \rightarrow \infty$), which implies in an infinitesimal ($\delta_H \rightarrow 0$ and $\delta_M \rightarrow 0$) or inexistent hydrodynamic and mass boundary layer surrounding the catalyst film. Thus, a constant and homogeneous concentration of species *i* in the liquid phase was assumed.

On the other hand, at the remaining boundaries the normal gradient of species *i* concentration was assumed as null, according to Eq. 3.12:

$$-\mathbf{n} \cdot \left(-D_{eff} \nabla c_i\right) = 0 \tag{3.12}$$

3.2.1.3 Complementary study: effect of the fluid phase on the solid phase performance

A complementary study was carried out to investigate the interaction of the liquid and solid phases in more details. Fluid flow was allowed in a microchannel interfacing the photocatalytic film. The velocity field within this flow channel was modeled through Navier-Stokes and mass conservation equations, expressed according to Eqs. 3.13 and 3.14, respectively:

$$\rho\left(\mathbf{u} \cdot \nabla\right)\mathbf{u} = \nabla \cdot \left[-p\mathbf{I} + \mu\left(\nabla\mathbf{u} + \left(\nabla\mathbf{u}\right)^T\right)\right] + \mathbf{F} \tag{3.13}$$

$$\rho \nabla \cdot \mathbf{u} = 0 \tag{3.14}$$

At the flow channel inlet, a Dirichlet boundary condition was applied (given velocity), according to Eq. 3.15:

$$\mathbf{u} = \mathbf{u}_0 \tag{3.15}$$

At the channel outlet, an atmospheric pressure boundary condition (null gauge pressure) was applied, according to Eq. 3.16:

$$p = 0 \tag{3.16}$$

In addition, the convection-diffusion equation (Eq. 3.17) was used to model the species *i* transport within the fluid phase:

$$\nabla \cdot \left(-D_i \nabla c_i \right) + \mathbf{u} \cdot \nabla c_i = 0 \tag{3.17}$$

At the channel inlet, the species *i* concentration was specified, according to Eq. 3.18:

$$c_i = c_{0,i} \tag{3.18}$$

Finally, at the channel outlet, the gradient of species *i* concentration was defined as zero, according to Eq. 3.19:

$$-\mathbf{n} \cdot \left(-D_i \nabla c_i \right) = 0 \tag{3.19}$$

3.2.2 Computational procedure

3.2.2.1 Photocatalytic film modeling

Light irradiance (at the wavelength λ = 365 nm) and reactive species transport inside the photocatalytic film was modeled with the finite element-based code COMSOL® Multiphysics (COMSOL® Inc, Burlington, MA), version 4.3a.

A two-dimensional rectangular domain (with height varying between δ = 100 nm and δ = 10 μm) was considered in all simulations. The entire domain was discretized with triangular mesh consisting of elements with maximum and minimum size of 5×10^{-8} m and 10^{-10} m, respectively, maintaining a maximum element growth rate of 1.1, resolution of curvature of 0.2 and resolution of narrow regions of 1.0.

The fully coupled system of equations was solved in steady state using Newton-Raphson iterations and MUMPS direct solver. A relative error of the numerical solutions below 10^{-3} was assumed as criterion for convergence.

The reaction rate was evaluated within the photocatalytic film according to Eq. 3.20, taking into account the line integral of the rate of disappearance of species *i* along the porous matrix thickness point-by-point. A unit cross sectional area normal to the photon flux (*A*) was considered.

$$r = A\int_0^{\delta} \eta k_{r,app} c_i I_{\lambda}^{\gamma} (1-\varepsilon) dy \tag{3.20}$$

Light intensities varying in the range $I_{\lambda,0}$ = (10-200) W·m^{-2} were considered. A normalized reaction rate (r/r_{max}) was computed for each case, taking into account the maximum rate of disappearance of species *i* (r_{max}) for each scenario evaluated.

The optimal film thickness was extracted from the simulations for the BSI and FSI mechanisms. In the case of BSI configuration, the maximum of the normalized reaction rate (r/r_{max}) was considered the optimal condition. On the other hand, in the case of FSI mechanism a cut-off value corresponding to 95% of r/r_{max} was taken as the optimal film thickness, since in this configuration a saturation of r/r_{max} is approached asymptotically.

A sensitive analysis was conducted to evaluate the effect of varying $k_{r,app}$, D_{eff} and κ_{λ} on the optimal film thickness. In particular, simulations were carried out taking into account ±50% of those parameters and δ_{opt} was calculated for each case.

MATLAB® (version R2010b 7.11.0.584) curve fitting toolbox was used to adjust equations for the prediction of the optimal film thickness (δ_{opt}) for the BSI and FSI mechanisms as a function of $I_{\lambda,0}$, $k_{r,app}$, D_{eff} and κ_{λ}. The Trust-Region algorithm was used for the nonlinear least squares minimization.

3.2.2.2 Complementary study

A complementary study was carried out to evaluate the effect of the fluid phase properties on the behavior of the solid phase (immobilized photocatalyst). A 2D microchannel with length of 100 μm was built and arranged in a way that one of its walls was located at the interface with the solid phase, which was allowed to vary its thickness within the limit previously established.

At the inlet of the flow channel a known average velocity was specified (laminar inflow condition, i.e., the flow was fully developed at

the entrance of the computational domain), while at the outlet an atmospheric pressure condition was applied (null gauge pressure). At the wall interfacing the immobilized photocatalyst the no-slip boundary condition was used and symmetry was considered at the remaining boundary.

Two configurations were evaluated regarding the flow channel width: i) considering the channel with fixed width of 10 μm along the entire simulation and ii) allowing the channel width to vary in order to achieve a fixed total width (flow channel + photocatalytic film) of 10 μm.

The entire computational domain was discretized with unstructured mesh. A mesh convergence study was conducted to ensure that the results are independent of the discretization level. The same mesh features and solver settings previously specified were retained.

The velocity at the flow channel inlet and the species *i* initial concentration were varied and the average species concentration at the channel outlet was calculated for each film thickness considered. Additionally, the reaction rate profiles within the solid phase (immobilized photocatalyst) were recorded for comparison with the results obtained when the fluid phase was neglected in the simulations.

3.3 RESULTS AND DISCUSSION

Figure 3.2 presents the normalized reaction rate (r/r_{max}) profiles within the photocatalytic film as a function of its thickness and the incident irradiation ($I_{\lambda,0}$). In all cases the wavelength λ = 365 nm was considered. Clearly, there is an inflection point corresponding to a global maximum in the curves obtained for the BSI mechanism. On the other hand, the curves approach a saturation value of r/r_{max} as the film thickness is increased in the case of FSI mechanism. In all scenarios, however, the normalized reaction rate profiles are dependent on the light irradiation intensity.

When the light intensity applied at the porous matrix surface was increased from $I_{\lambda,0} = 10\ \mathrm{W{\cdot}m^{-2}}$ to $I_{\lambda,0} = 200\ \mathrm{W{\cdot}m^{-2}}$ there was a shift of the global maximum of r/r_{max} for the BSI mechanism towards lower film thicknesses. The same scenario can be observed for the FSI case, although it was less noticeable due to the asymptotic behavior of the r/r_{max} curves.

When the BSI mechanism is considered, as the film thickness is increased for $\mathrm{d}(r/r_{max})/\mathrm{d}(\delta) > 0$ the gain in surface area available for chemical reaction is higher than the increase in the resistance to diffusion and light transport. At the point where $\mathrm{d}(r/r_{max})/\mathrm{d}(\delta) = 0$, the contribution

Figure 3.2: Normalized reaction rate (r/r_{max}) as a function of the photocatalytic film thickness (δ) and the incident irradiation intensity ($I_{\lambda,0}$) for (a) BSI and (b) FSI mechanisms.

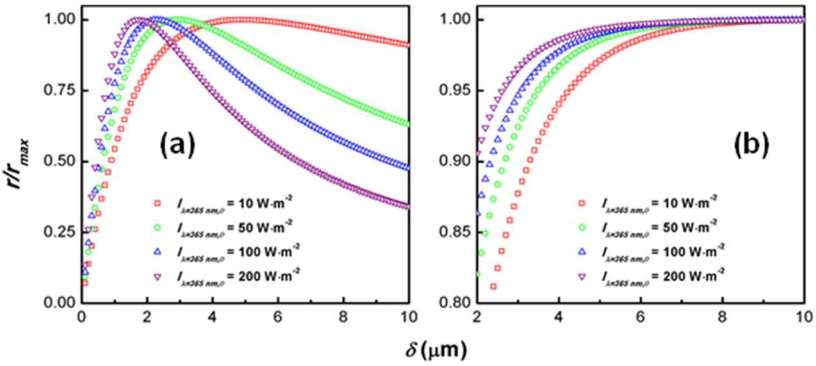

Figure 3.3: Concentration profiles for the BSI mechanism: (a) $I_{\lambda,0}$ = 10 W·m^{-2} and (b) $I_{\lambda,0}$ = 200 W·m^{-2}. Concentration profiles for the FSI mechanism: (c) $I_{\lambda,0}$ = 10 W·m^{-2} and (d) $I_{\lambda,0}$ = 200 W·m^{-2}. Normalized irradiation distribution (e) within the film. Comparison of BSI and FSI concentration profiles within the film (f) for $I_{\lambda,0}$ = 200 W·m^{-2}.

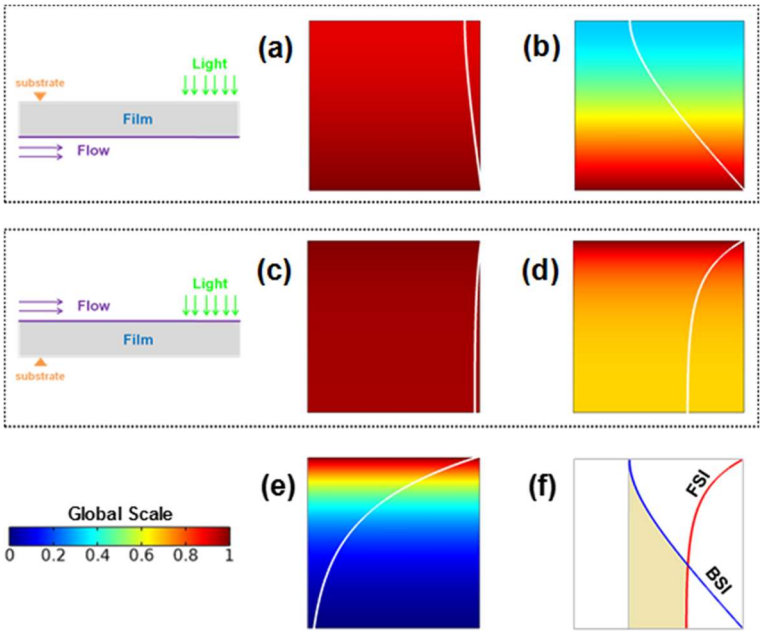

of these conflicting factors is exactly balanced. Nevertheless, when $d(r/r_{max})/d(\delta) < 0$ as the film thickness is increased there is a higher gain in resistance to diffusion and photon transport within the film of photocatalyst than in surface area available to chemical reaction.

On the other hand, for the FSI scheme there is no competition of controlling mechanisms as the film thickness is increased. As δ becomes higher, the surface area available for chemical reaction and the resistance to diffusion and light transport within the film always increase. However, for low values of δ, as the film thickness is increased $d(r/r_{max})/d(\delta) > 0$ and a significant extension of the material is effectively used in the photocatalytic reaction. Conversely, for high δ, $d(r/r_{max})/d(\delta) \rightarrow 0$ as the film thickness is increased since a substantial amount of material becomes ineffective in the photocatalytic reaction.

Figure 3.3 illustrates the irradiation and species concentration profiles within a photocatalytic film with $\delta = 5$ μm (taken as reference) illuminated according to the BSI and FSI mechanisms. In particular, Figures 3.3a and b present the species concentration profile within the film irradiated with the BSI mechanism considering $I_{\lambda,0} = 10$ W·m^{-2} and $I_{\lambda,0} = 200$ W·m^{-2}, respectively. Additionally, Figures 3.3c and d present the species concentration profile within the film subjected to the FSI arrange, considering $I_{\lambda,0} = 10$ W·m^{-2} and $I_{\lambda,0} = 200$ W·m^{-2}, respectively.

Figure 3.3e shows the normalized irradiation profile within the photocatalytic film. This profile is independent of the incident irradiation. Clearly, a logarithmic attenuation of the light intensity occurs within the film. In fact, strong light absorption can be obtained as the film thickness is increased (see Figure 3.4). This fact indicates the importance of working at optimal conditions when designing immobilized reactors, especially in the case of microfluidic devices, where a mixture of BSI and FSI is frequently observed.

When the BSI mechanism is considered, a higher variation of the concentration profiles was observed for both incident irradiations taken into account (i.e., $I_{\lambda,0} = 10$ W·m^{-2} and $I_{\lambda,0} = 200$ W·m^{-2}). In all cases, however, a clear exponential variation of species *i* concentration within the film can be noticed. Figure 3.3f presents a direct comparison of the concentration profiles obtained when the BSI and FSI mechanisms are considered keeping the operational conditions constant ($\delta = 5$ μm and $I_{\lambda,0} = 200$ W·m^{-2}). A higher variation of species *i* concentration profile can be explicitly observed, i.e., the BSI mechanism results in a more pronounced degree of species *i* conversion within the film, resulting in a more efficient utilization of the photocatalytic material.

Figure 3.4: Attenuation (%) of the irradiation intensity as a function of the photocatalytic film thickness (δ).

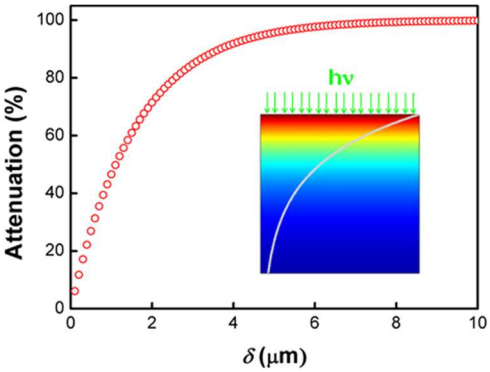

It should be considered that the film thickness influences three competing factors taking place in immobilized photocatalytic reaction systems: i) the area available for the chemical reaction (which essentially takes place at the active sites), ii) the transport of the solute and charge carriers (electrons and holes) within the porous matrix and iii) the light distribution. When the thickness (δ) is increased, there is an increase in the total area available for the chemical reaction. On the other hand, the resistance to the species diffusion through the porous matrix, as well as for the electron/hole transport within the film, is increased. In addition, the light attenuation is more pronounced as the film thickness is increased (according to Beer-Lambert's law). All these factors, essentially coupled, lead to the existence of an optimal film thickness, which should be considered in the design of photochemical reactors with immobilized film for the maximization of the catalyst's performance.

Figures 3.5a and b present the optimal film thickness (δ_{opt}) as a function of the incident irradiation ($I_{\lambda,0}$) for the BSI and FSI mechanisms, respectively. A sensibility analysis was also carried out, varying the apparent first-order reaction constant ($k_{r,app}$), the effective diffusivity (D_{eff}) and the absorption coefficient (κ_λ) by ±50%, to assess the influence of changes in the intrinsic kinetics, the transport properties of the fluid (D_i), the properties of the porous matrix (ε and τ) and the optical features of the material.

It should be highlighted that properties of the fluid phase, i.e., velocity and species i concentration, do not influence the optimal thickness of the solid phase (immobilized photocatalyst). Figure 3.6

presents the species *i* concentration contours for three distinct photocatalytic film thicknesses, keeping the total width of the system (flow channel + photocatalytic film), the fluid average inlet velocity, the concentration at the channel inlet and the light incident irradiation constant (u_0 = 1 mm·s^{-1}, $c_{0,i}$ = 1 mg·L^{-1} and $I_{\lambda,0}$ = 100 W·m^{-2}, respectively).

Additionally, Figure 3.7 shows the average species *i* concentration at the flow channel outlet as a function of the inlet velocity (u_0 = 0.5, 1.0 and 1.5 mm·s^{-1}, respectively) and inlet concentration ($c_{0,i}$ = 0.5, 1.0 and 1.5 mg·L^{-1}, respectively) considering a microchannel with fixed width.

It can be clearly noticed from Figure 3.7a that the average species concentration taken at the channel outlet (fluid phase) reached a point of minimum when the photocatalytic film thickness was varied. Interestingly, this point corresponds exactly to the same film thickness regardless the velocity applied at the channel inlet. Moreover, the same behavior was noticed when the species *i* inlet concentration was varied. When taking the average species *i* concentration at the channel outlet, a point of minimum was observed varying the photocatalytic film thickness. Again, this point was reached exactly at the same film thickness regardless the concentration specified at the channel inlet. This behavior can be observed in Figure 3.7b-d.

Figure 3.5: Optimal film thickness (δ_{opt}) as a function of the incident irradiation ($I_{\lambda,0}$) and systematic variations of the apparent first-order reaction constant ($k_{r,app}$), the effective diffusivity (D_{eff}) and the absorption coefficient (κ_λ) for the (a) BSI and (b) FSI mechanisms.

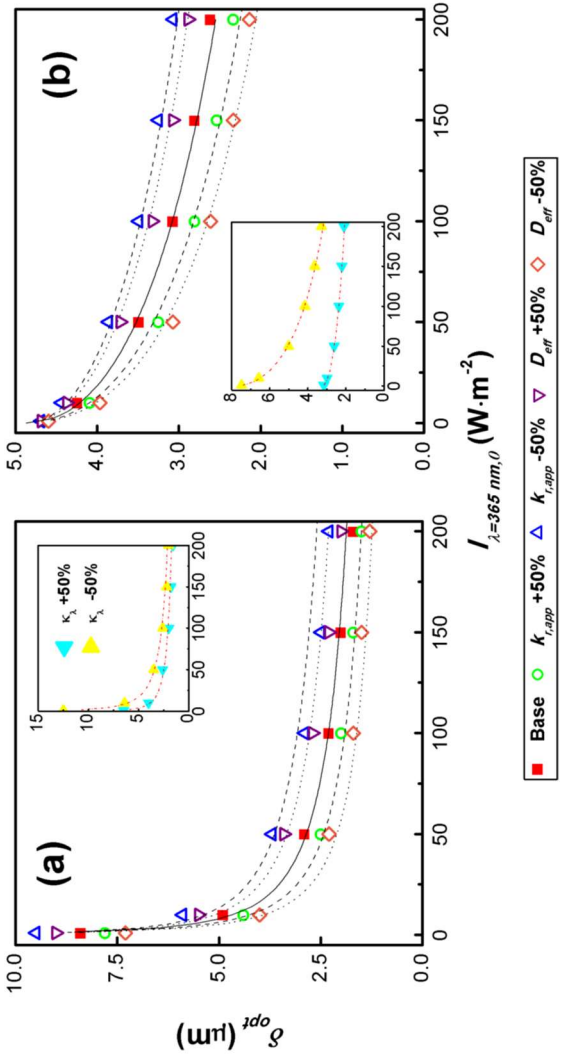

Figure 3.6: Contours of species *i* concentration as a function of the photocatalytic film thickness for a solid-liquid system (flow channel interfacing the active catalyst layer) subjected to the BSI mechanism: (a) $\delta = 1$ µm, (b) $\delta = 5$ µm and (c) $\delta = 10$ µm. In all cases $I_{\lambda,0} = 100$ W·m^{-2}, $c_{0,i} = 1.0$ mg·L^{-1} and $u_0 = 1$ mm·s^{-1}.

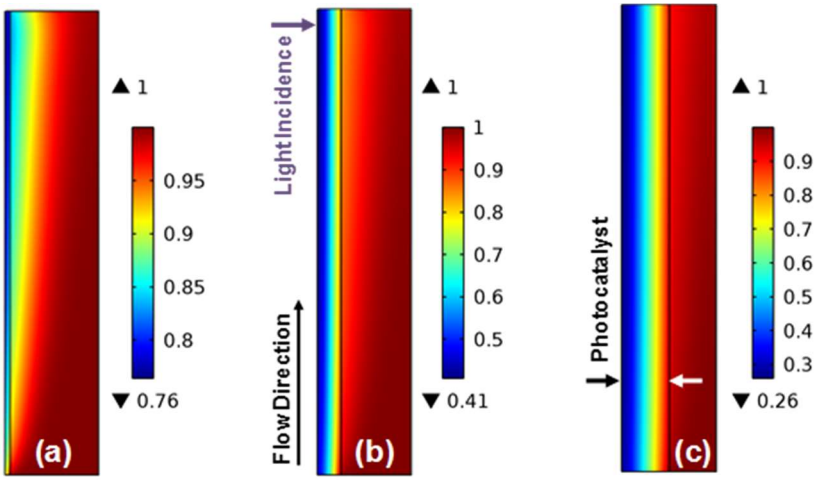

It should be highlighted that when fixing the flow channel width, the point of minimum observed for the average species concentration at the outlet as a function of the photocatalytic film thickness corresponds exactly to the same optimal thickness computed when evaluating the r/r_{max} profiles within the solid phase (photocatalyst layer). In fact, considering the fluid phase in the simulations did not alter the r/r_{max} behavior within the solid phase in any case evaluated.

Also, if the liquid phase is neglected and only the solid phase is considered in the simulations (applying the species concentration at the virtual solid-liquid interface as a Dirichlet boundary condition) the same behavior for r/r_{max} is retained, leading to exactly the same optimal film thickness as a function of the incident irradiation ($I_{\lambda,0}$), the apparent first-order reaction constant ($k_{r,app}$), the effective diffusivity (D_{eff}) and the absorption coefficient (κ_λ).

On the other hand, if the fluid phase is considered and the total width of the system (flow channel + photocatalytic film) is assumed as constant, the r/r_{max} profiles within the solid phase remain the same (indicating identical optimal thickness) but slight variations of the location of the point of minimum in the profiles of average species concentration at the outlet of the flow channel as a function of δ are

observed. However, these minimal changes do not represent a shift of the optimal reaction conditions within the photocatalytic film, but result from the computation of the average concentration at the outlet considering a varying reference (in this case the flow channel width is different for each value of δ simulated).

Figure 3.7: Average species *i* concentration at the flow channel outlet as a function of (a) the velocity at the inlet and the initial concentration at the channel inlet: (b) 0.5, (c) 1.0 and (d) 1.5 mg·L^{-1}.

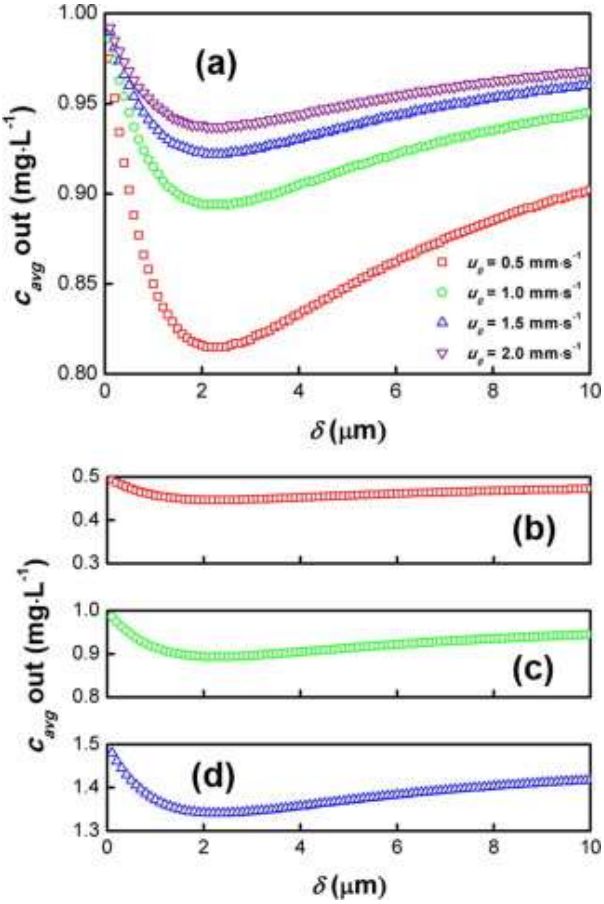

Therefore, based on these observations, it is possible to affirm that the optimal photocatalytic film thickness depends only on properties

within the solid domain (incident light intensity, apparent first-order reaction constant, species effective diffusivity and absorption coefficient). The fluid phase has none effect on the optimal conditions of the immobilized photocatalytic film.

Based on this scenario, a correlation for the prediction of the optimal TiO_2 film thickness (δ_{opt}) as an explicit function of the incident irradiation ($I_{\lambda,0}$), the apparent first-order reaction constant ($k_{r,app}$), the effective diffusivity (D_{eff}) and the absorption coefficient (κ_λ) was developed and is summarized in Eqs. 3.21 and 3.22 for the BSI and FSI schemes, respectively.

$$\begin{aligned}\delta_{opt}^{BSI}\ (\mu m) = &\left(23.81\cdot\kappa_\lambda^{-0.2193} - 16.98\right)\\ &\cdot I_{\lambda,0}^{\left(0.28\cdot\kappa_\lambda^{0.331} - 0.5442\right)} \cdot I_{\lambda,0}^{\left(-0.55\cdot k_{r,app}^{0.264} + 0.3695\right)}\\ &\cdot I_{\lambda,0}^{\left(-2.042\times10^{19}\cdot D_{eff}^2 + 4.42\times10^{9}\, D_{eff} - 0.1946\right)}\end{aligned} \tag{3.21}$$

$$\begin{aligned}\delta_{opt}^{FSI}\ (\mu m) = &\left(13.9\cdot\kappa_\lambda^{-0.2615} - 10.84\right)\\ &\cdot\left(-0.02651\cdot\kappa_\lambda^2 + 0.08238\cdot\kappa_\lambda + 0.9147\right)^{\sqrt{I_{\lambda,0}}}\cdot\\ &\cdot\left(-0.08895\cdot k_{r,app}^{0.4255} + 1.047\right)^{\sqrt{I_{\lambda,0}}}\\ &\cdot\left(1.673\cdot D_{eff}^{0.02192}\right)^{\sqrt{I_{\lambda,0}}}\end{aligned} \tag{3.22}$$

In Eqs. 3.21 and 3.22, $I_{\lambda,0}$, $k_{r,app}$, D_{eff} and κ_λ must be inserted with unities of $W\cdot m^{-2}$, s^{-1}, $m^2\cdot s^{-1}$ and μm^{-1}, respectively. This correlation is valid for $I_{\lambda,0} < 250\ W\cdot m^{-2}$ and ($k_{r,app}$, D_{eff}, κ_λ)±100%.

These equations can be readily used for the design of immobilized photocatalytic reactors considering the BSI and FSI mechanisms (e.g., it can be used in optimization algorithms that takes into account the effect of the illumination arrange on the photochemical reactor design). It should be noted that different reaction systems can be readily evaluated by changing the pseudo first-order reaction constant ($k_{r,app}$) and the effective diffusivity (D_{eff}) accordingly. Thus, the correlations proposed herein can be used for liquid and gaseous systems considering reactions of synthesis and degradation (pollution control).

It should be highlighted that Eqs. 3.21 and 3.22 were obtained from curve fitting to data derived from computational simulation. Good

fitting was obtained due to the high number of parameters present in each equation. This high number of adjustable parameters arose from the need to obtain equations able to satisfactorily account for the different variables considered ($I_{\lambda,0}$, $k_{r,app}$, D_{eff} and κ_λ). In particular, a distinct behavior was encountered for the optimal film thickness as a function of the absorption coefficient (κ_λ) for different incident irradiation ($I_{\lambda,0}$) when compared to the profiles obtained for the effective diffusivity (D_{eff}) and the apparent pseudo-first order reaction constant ($k_{r,app}$). Also, different functional forms were encountered for the BSI and FSI mechanisms. Obviously, using a high number of adjusted parameters allowed a good representation of the trend of δ_{opt} as a function of $I_{\lambda,0}$, $k_{r,app}$, D_{eff} and κ_λ for both illumination mechanisms evaluated (BSI and FSI). However, care should be taken when using these equations and special attention should be given to their limits of validity.

3.4 CONCLUSIONS

Immobilized photocatalytic systems offer the advantage of dispensing post-treatment for recovery of the photocatalyst nanoparticles. However, this configuration is usually limited by significant mass and photon transport resistances when applied to conventional equipment. Nevertheless, great effort has been devoted to the intensification of chemical processes at micro and nano-sized devices, which can combine the intrinsic advantages of immobilized photocatalyst with excellent mass and photon transport characteristics, allowing the design of solutions suitable for large-scale applications.

When designing immobilized photocatalytic systems, two illumination mechanisms should be considered: backside illumination (BSI) and front-side illumination (FSI). In each case, different interaction between the irradiation intensity and species concentration profiles are observed within the photocatalytic film. The FSI and BSI mechanisms can be compared with co-current and counter-current operation modes in traditional chemical processes.

For each illumination mechanism, there is an optimal film thickness that should be considered for the optimization of the reactor performance. In the BSI scheme there is an inflection point at which the maximum reaction rate is observed, while in the FSI arrange the maximum rate of reaction is approached asymptotically. Also, this phenomenon is governed by the incident irradiation ($I_{\lambda,0}$), the apparent first-order reaction constant ($k_{r,app}$), the effective diffusivity (D_{eff}) and the

absorption coefficient (κ_λ) that characterize the reaction system within the photocatalytic layer. Properties of the fluid phase were found to not influence the optimal thickness of the immobilized material.

In this work, an explicit correlation allowing the prediction of the optimal film thickness in immobilized photocatalytic systems for BSI and FSI arranges taking into account the main parameters that govern the process was found. These equations can be readily used in optimization algorithms for the design of immobilized photocatalytic reactors at different scales.

3.5 IMPRESSIONS AND PERSPECTIVES

The main difficulty encountered during the development of the research reported in this chapter was the identification of equations able to take into account the effect of $I_{\lambda,0}$, $k_{r,app}$, D_{eff} and κ_λ on the optimal film thickness to be deposited on the walls of microfluidic devices. As a direct consequence, the main limitation of the research reported herein can be identified: the correlation obtained relies on several adjustable parameters, which limits its application as indicated in section 3.3. Moreover, it should be considered that Eqs. 3.21 and 3.22 were obtained from fitting to data obtained from numerical simulations. Therefore, care should be taken when applying them and further studies aiming to investigate the accuracy of these equations through experimental validation should be carried out.

Moreover, it should be considered that some assumptions were made when deriving the computational model used in this chapter. For instance, the porosity of the material was assumed as constant. Moreover, the effect of defects caused by the introduction of a doping agent on the TiO_2 film was not considered. Further research should be conducted aiming to investigate the effect of varying material properties and the introduction of a doping agent on the optimal film thickness of photocatalyst immobilized on the walls of microfluidic devices. When considering the introduction of a doping agent the effect of light scattering, for instance, could become relevant and should be considered in the model. This is an interesting and vast field to be explored in further investigations.

4. NUMERICAL SIMULATION OF ISOTHERMAL GAS-LIQUID FLOW PATTERNS IN MICROCHANNELS WITH VARYING WETTABILITY

This chapter is based on the paper entitled "Numerical Simulation of Isothermal Gas-Liquid Flow Patterns in Microchannels with Varying Wettability" (*Chemical Engineering Research and Design*, Volume 109, May 2016, Pages 698–706), by Natan Padoin, Alan Zago de Souza, Karoline Ropelato and Cíntia Soares. Abstract, keyworkds, acknowledgements and references were omitted.

4.1 INTRODUCTION

Along the last decades, microchannel technology has flourishing as an interesting route to process intensification (LAM *et al.*, 2013; SHAO *et al.*, 2009; THOME *et al.,* 2013). Microchannels allow improved heat and mass transfer and reaction rates due to their significantly high surface-to-volume ratio (LAM *et al.*, 2013). Microreactors, for instance, have a surface-to-volume ratio varying in the range of 10,000 to 50,000 $m^2 \cdot m^{-3}$, while in conventional equipment this ratio is approximately 100 $m^2 \cdot m^{-3}$ and rarely they can reach 1,000 $m^2 \cdot m^{-3}$ (JÄHNISCH *et al*., 2004). Moreover, these microstructured unities are characterized by low Reynolds number (LAM *et al.*, 2013) (usually laminar conditions are established), short diffusion path, fast mixing (MATSUSHITA *et al.*, 2008) and excellent controllability, allowing process optimization with a minimal waste disposal. Thus, microchannel technology has been used for efficient process development in an environmentally friendly way.

The operation of microfluidic devices frequently involves flow of two or more phases (WÖRNER, 2012), particularly gas-liquid flow in the case of microdistillation, microabsorption, microstripping and microreaction, and liquid-liquid flow in the case of microextraction. However, according to Shao *et al*. (2009), the methods established for the prediction of two-phase flow patterns in conventional equipment do not readily apply to microfluidic unities. Several factors, such as the increased importance of the contact angle along with the flow confinement, influence on this scale separation. In fact, at the microscale multiphase flow behaves similarly to flow under microgravity at the macroscale and, thus, the gravitational forces frequently become negligible in microchannels.

This scenario has pointed out in the direction of developments on the basis of understanding and predicting two-phase flow boundaries at microscale. From a pragmatic point of view, the prediction of the flow pattern that arises from a singular combination of interacting phases has an immense interest, since different morphologies result in different area concentration available for momentum, heat and mass exchanges across the interface. Thus, the pressure drop and the separation or heat recovery efficiencies can be more adequately estimated.

According to Shao *et al.* (2009), six flow patterns can be observed in microchannels: bubbly and Taylor flow (surface tension dominated), churn and Taylor-annular flow (transitional) and dispersed and annular flow (inertia dominated). However, this classification is not standardized and several bifurcations have been proposed. For instance, while several works do not consider the existence of stratified flow pattern in microchannels, this flow morphology has been indeed reported (CHOI *et al.*, 2011; SANTOS and KAWAJI, 2010).

In general, the Taylor (or slug) flow regime has been the configuration most extensively addressed in the literature for the scenario where isothermal condition is assumed. Qian and Lawal (2006) studied Taylor slug flow in 2D and 3D microchannels with T-junction and observed that there is an increased non-uniformity of the slug length throughout the channel as the cross-sectional area and the gas or liquid flow rates are increased. The authors also observed that gravitational effects and fluid properties (particularly density and viscosity) have no importance in flow at microscale. Gupta *et al.* (2009) used CFD to simulate isothermal Taylor flow in a two-dimensional axisymmetric horizontal microchannel. The authors primarily aimed to address the existence of a liquid film at the wall. Abadie *et al.* (2012) studied experimentally and numerically (on a 2D domain) the effect of fluid properties and operational conditions on the formation of slugs in microchannels. Dai *et al.* (2009) and Guo and Chen (2009) worked on the numerical investigation of the mechanisms that control slugs formation during gas-liquid flow in T-junction microchannel. Additionally, Shao *et al.* (2008) and Sobieszuk *et al.* (2010) investigated the length of bubbles formed during the development of slug flow in microchannels.

Accordingly, few works dealt with the numerical simulation of gas-liquid flow regimes apart from the slug flow in microchannels. Santos and Kawaji (2010) investigated experimentally and numerically gas-liquid flow in nearly square microchannels with 113 μm hydraulic diameter and with air and water superficial velocities varying in the range

(0.018–0.791) $m \cdot s^{-1}$ and (0.042–0.757) $m \cdot s^{-1}$, respectively. The slug and stratified flow patterns were observed. In addition, the role of the contact angle specified at the channel walls on the gas-liquid flow morphology has not been extensively addressed. In fact, at the microscale (where the importance of superficial properties is more pronounced than that related to the bulk) a variation in the contact angle, making the surface hydrophilic or hydrophobic, may alter the flow pattern developed. Thus, it can significantly affect the performance of the system. As an example, this analysis is important for the design of monolithic reactor channels considering different catalysts immobilized on the active walls.

Additionally, it should be highlighted that most of these works do not consider the evolution of the numerical solution until the statistical steady state is reached. Milioli and Milioli (2010) present a discussion on the importance of considering the results at the statistical steady state regime when interpreting data from numerical simulation of multiphase flow (particularly fluidized beds in their study). Briefly, the numerical evaluation of multiphase flow is inherently a statistical process and, therefore, the time-advancement of the flow variables should be considered in the assessment of the system behavior in order to proper project the equipment.

In this study, isothermal flow patterns developed in a rectangular microchannel were evaluated through the volume of fluid (VOF) model. In particular, this work elucidated that CFD can be used for the evaluation of the impact of variation of the wall wettability on isothermal gas-liquid flow patterns developed in microchannels. The numerical results were evaluated with the data obtained by Choi *et al.* (2011). A comparison between numerical and experimental data and some available correlations showed good agreement. Thus, computational simulations can be used as a source of a-priori information on the flow expected in microfluidic devices, which affects the design and optimization techniques applied to compact devices and process intensification strategies.

4.2. METHOD

4.2.1 Mathematical model

The gas-liquid flow in the microchannels was solved through the volume of fluid (VOF) model. In particular, the interface between the gas and liquid phases was solved through the volume fraction conservation equation for the secondary phase (liquid, in this case), according to Eq. 4.1 (FLUENT, 2013):

$$\frac{\partial}{\partial t}\left(\alpha_l \rho_l\right) + \nabla \cdot \left(\alpha_l \rho_l \mathbf{v}\right) = 0, \tag{4.1}$$

where t is time (s), α is the volume fraction (dimensionless), ρ is the density (kg·m^{-3}), $\mathbf{v}$ is the velocity vector (m·s^{-1}) and the subscript l indicates liquid phase. Additionally, the volume fraction of the gas phase can be obtained by solving the restriction equation expressed by Eq. 4.2 (FLUENT, 2013):

$$\alpha_l + \alpha_g = 1 \tag{4.2}$$

A single pressure and velocity field is shared by the liquid and gas phases through a unique momentum conservation equation, represented by Eq. 4.3 (FLUENT, 2013):

$$\begin{aligned}\frac{\partial}{\partial t}\left(\rho \mathbf{v}\right) + \nabla \cdot \left(\rho \mathbf{v}\mathbf{v}\right) = -\nabla p + \nabla \cdot \left[\mu\left(\nabla \mathbf{v} + \nabla \mathbf{v}^{\mathbf{T}}\right)\right] \\ + \sigma\kappa \frac{\rho \nabla \alpha_g}{1/2\left(\rho_l + \rho_g\right)},\end{aligned} \tag{4.3}$$

where ρ is the mixture density (kg·m^{-3}), $\mathbf{v}$ is the mixture velocity vector (m·s^{-1}), p is the pressure field (kg·m·s^{-2}), μ is the mixture dynamic viscosity (kg·m·s^{-1}), σ is the surface tension at the gas-liquid interface (kg·s^{-2}), κ is the interface curvature (m^{-1}), α is the volume fraction (dimensionless) and the subscripts l and g indicates liquid and gas phase, respectively. The mixture density and dynamic viscosity were solved through a volume-weighted mixture law expressed by Eq. 4.4 (FLUENT, 2013):

$$\begin{aligned}\rho &= \alpha_g \rho_g + \left(1 - \alpha_g\right)\rho_l \\ \mu &= \alpha_g \mu_g + \left(1 - \alpha_g\right)\mu_l\end{aligned} \tag{4.4}$$

The interface curvature κ was computed through the model of Brackbill *et al.* (1992). Using this method, κ is calculated as the divergent

of the unit vector normal to the interface, according to Eq. 4.5 (FLUENT, 2013):

$$\kappa = \nabla \cdot \hat{n}, \tag{4.5}$$

where the vector normal to the interface and its unit correspondent are given by Eqs. 4.6 and 4.7, respectively (FLUENT, 2013):

$$n = \nabla \alpha_l \tag{4.6}$$

$$\hat{n} = \frac{n}{|n|} \tag{4.7}$$

At the cells adjacent to the walls, the unit normal vector (Eq. 4.7) is modified by the specified contact angle, according to Eq. 4.8 (FLUENT, 2013):

$$\hat{n} = \hat{n}_w \cos\theta_w + \hat{t}_w \sin\theta_w, \tag{4.8}$$

where $\hat{\boldsymbol{n}}_{\boldsymbol{w}}$ is the unit vector perpendicular to the wall, $\hat{\boldsymbol{t}}_{\boldsymbol{w}}$ is the unit vector tangential to the wall and $\boldsymbol{\theta_w}$ is the specified contact angle. Values of $\boldsymbol{\theta_w} < 90°$ represent a hydrophilic or wetting wall, while $\boldsymbol{\theta_w} > 90°$ is used to describe a hydrophobic or non-wetting wall. Thus, the specified contact angle at the walls directly affect the fluid flow within the device modifying the interface curvature (κ) and, consequently, the velocity and pressure fields (according to Eq. 4.3).

Finally, it should be noted that in this study the flow patterns were evaluated at isothermal conditions, i.e., there was no need to solve the energy conservation equation. Additionally, the effect of mass transfer across the fluidic interface was neglected.

4.2.2 Computational procedure

The numerical simulations were based on the experimental setup investigated by Choi *et al.* (2011). In particular, similar geometrical and flow feeding conditions adopted by the authors were used as reference for the computations. In all cases the microchannel width (W = 617 μm and W = 608 μm, for the cases *phylic* and *phobic*, respectively) was smaller than the Laplace constant (λ = 2.7 mm). The constant λ indicates the

balance between surface tension and gravitational forces and represent a threshold for the separation between microchannels and conventional channels. The CFD simulations were performed in the commercial code ANSYS® CFD (Fluent®), version 15.0, in the two-dimensional domain presented in Figure 4.1.

Figure 4.1: Computational domain used in the CFD simulations. (a) characteristic dimensions and boundary conditions and (b) mesh details are highlighted. A complementary study was carried out with the domain shown in (c) to elucidate the sensitivity in varying the wall contact angle.

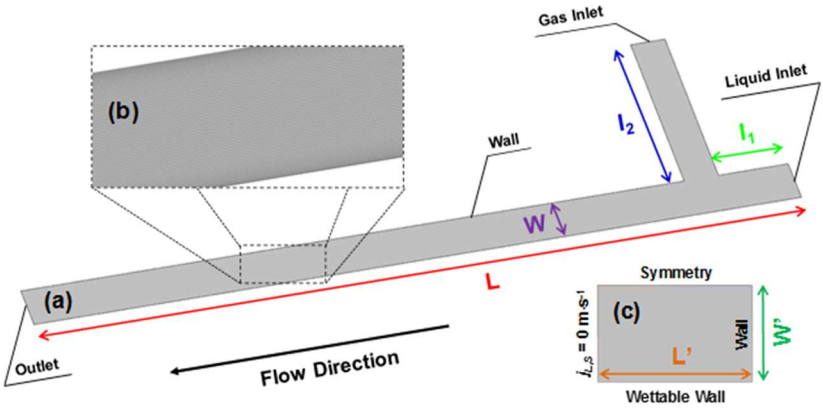

The main microchannel length (L) consisted of 12.5 mm. This value corresponds to 25% of the length of the experimental device used as reference. The gas and liquid streams were fed to the mixing section through perpendicular channels with 2.5 mm (l_1) and 1.25 mm (l_2), respectively, which correspond to a reduction of 87.5% regarding to the experimental setup for both cases. The width of the microchannel (main and inlet sections) varied according to the wall wettability in order to comply with the experimental platform. Therefore, in the hydrophilic case (*phylic*) the dimension W was specified as 617 μm, while in the hydrophobic case (*phobic*) W assumed the value 608 μm.

Normal uniform velocity was specified for the gas (primary phase, $j_{in,G}$ = 0.07 m·s^{-1}) and liquid (secondary phase, $j_{in,L}$ = 0.19 m·s^{-1}) streams at their respective inlets while null (gauge) pressure (p_0) was defined at the outlet. No-slip boundary condition was used at the walls. Pure water (H_2O) and nitrogen (N_2) were used as working fluids, with physical properties indicated in Table 4.1.

Table 4.1: Properties of the fluids used in the numerical simulations.

Fluid	ρ (kg·m^{-3})	μ (kg·m^{-1}·s^{-1})
Water	998.2	1.003×10^{-3}
Nitrogen	1.138	1.663×10^{-5}

The fluids were fed at room temperature and the flow was developed under isothermal conditions. All cases were initialized with a hybrid method and the liquid volume fraction was set as $\alpha_l = 1.0$ along the main channel. The surface tension at the gas-liquid interface was set as $\sigma = 0.072$ N·m^{-1}. Moreover, the wall contact angle was specified as $\theta_w = 25°$ and $\theta_w = 105°$ for the hydrophilic (*phylic*) and hydrophobic (*phobic*) cases, respectively. The effect of gravity acceleration was not taken into account in the simulations. As highlighted in section 4.1, under certain conditions multiphase flow in microchannels is not significantly sensitive to the gravitational field and neglecting it does not result in considerable impact on the flow pattern. It should be noted that the same feeding conditions were adopted for the *phylic* and *phobic* cases and only the contact angle specified at the walls was varied (along with the slight variation of dimension *W*, according to Figure 4.1, to comply with the experimental platform geometry).

The entire two-dimensional computational domain was discretized with quadrilateral mesh resulting in a structured grid refined at the walls with a smooth growth towards the center (see Figure 4.1b). The final mesh was smoothed in Fluent (with 2 iterations). A mesh refinement study was carried out taking the *phylic* case as reference. In this case, Taylor flow was expected and the liquid film developed between the microchannel walls and the cavities should be properly captured (GUPTA *et al.*, 2009). A reduced domain was used allowing evaluating the evolution of a single gas cavity. The optimal mesh defined for the *phylic* case was adopted for the *phobic* case simulations for coherence.

The discretization of the governing equations was performed with the finite volume method (FVM) through a pressure-based solver. The pressure–velocity coupling was solved in a segregated fashion with the PISO algorithm. The gradients were evaluated with the least squares cell-based method. In addition, the PRESTO! and second-order upwind schemes were used for the spatial discretization of pressure and momentum, respectively. The compressive algorithm (with second order accuracy) was adopted for the volume fraction spatial discretization. Finally, a first-order implicit scheme was used for the transient

formulation. This set of solver configurations were used to minimize spurious currents at the interface. All the sub-relaxation factors were maintained at their default values, i.e., 0.3, 1.0, 1.0 and 0.7 for pressure, density, body forces and momentum, respectively.

The flow was solved through a real transient formulation, in which the Courant–Friedrichs–Lewy (CFL) condition was adopted as the criterion for the time-step definition, according to Eq. 4.9 (FLUENT, 2013):

$$\Delta t = \frac{Co \times \Delta x}{\mathbf{v}}, \tag{4.9}$$

where Co is the Courant number (dimensionless), Δx is the cell length (m) and v is the fluid velocity ($m \cdot s^{-1}$).

In particular, $Co = 0.25$ was adopted for the determination of the time-step for the solution of the volume fraction equation in all simulations. Furthermore, the global value $Co = 2.0$ was adopted for the solution of the other conservation equations. This strategy yielded time-steps in the order of 10^{-5}-10^{-6} s. The convergence criterion adopted was absolute residuals less than 0.001 for the mass and momentum (x and y velocity components) conservation equations or 50 iterations per time step, whichever was reached first.

The statistical temporal variability of the simulations was evaluated. Time-averaged velocity profiles were adopted as criterion. According to Milioli and Milioli (2010) the statistical steady state is achieved when the time-averaged profiles of a certain parameter do not vary by a significant extent. In particular, time-averaged velocity profiles extracted from a mid-line crossing the main channel in the *phylic* case and three lines perpendicular to the main channel (located at 3.0, 7.5 and 12 mm from the liquid inlet) in the *phobic* case were used as reference. The time-averaged profiles were taken into account after the completion of the stabilized first residence time in the devices. All profiles were collected in time intervals corresponding to half of the residence time of the *phylic* case ($\Delta t = 0.02375$ s).

4.2.3 Model evaluation

The numerical results were evaluated by comparison with the experimental data obtained by Choi *et al.* (2011). The flow pattern morphologies were compared with the images obtained experimentally.

Moreover, quantitative data was obtained for the maximum length and surface area of the gas cavities generated in the *phylic* case and the thickness of the gas film developed in the *phobic* case, which were also compared with the experimental results. In particular, the maximum cavity length and surface area were determined by pixel-metering the flow pattern images obtained from the work of Choi *et al.* (2011) and the numerical results obtained in this work through the software ImageJ (SCHNEIDER, *et al.*, 2012).

Additionally, the pressure drop per cavity (ΔP_C, in the *phylic* case) was obtained at the mid-line of the computational domain (aligned with the main channel) and compared with the predictions obtained from the correlation developed by Choi *et al.* (2011), enunciated according to Eq. 4.10:

$$\Delta P_C = 0.2 u_C^{1.36}, \tag{4.10}$$

where u_C is the velocity of the cavity ($m \cdot s^{-1}$), defined according to Eq. 4.11:

$$u_C = C_1 J, \tag{4.11}$$

where C_1 is the ratio of cavity velocity and total superficial velocity and J is the total superficial velocity ($m \cdot s^{-1}$). The parameter C_1 was defined by Choi *et al.* (2011) as 1.14. However, different values of this parameter can be found in the literature, ranging from $C_1 = 1.0$ (CUBAUD and HO, 2004) to $C_1 = 1.2$ (CHUNG and KAWAJI, 2004).

4.2.4 Complementary study

A complementary study was performed in a simplified rectangular domain (length of 3 mm and height of 308.5 μm) to investigate the sensibility of varying the wall contact angle suppressing external convective contributions.

Figure 4.1c presents an overview of the boundary conditions applied. Null velocity was imposed at the left boundary, symmetry was used at the top boundary, while a no-slip wall condition was assigned at the remaining boundaries. In particular, the bottom wall was considered wettable and the same contact angles employed in the investigation of the numerical platform based on the work of Choi *et al.* (2011) were

considered, i.e., θ_w = 25° and θ_w = 105° for the hydrophilic and hydrophobic surfaces, respectively.

Overall, the same procedure described in section 4.2.2 was employed, despite some particularities discussed as follows. At t = 0 s the liquid volume fraction was set as α_l = 1.0 at (0 < L' < 1) mm and (0 < W' < 308.5) μm (see Figure 4.9a for reference). The entire domain was discretized with quadrilateral cells with 5 μm. The solution marched until t = 1 ms (0.001 s) with a fixed time step size of 1×10^{-6} s. At the final of the simulation a stabilized interface was reached, approaching the hydrodynamic equilibrium asymptotically.

4.3 RESULTS AND DISCUSSION

4.3.1 Dimensional analysis of the two-phase flow in the microchannels

Relevant dimensionless groups, namely Eötvös (*Eö*), Reynolds (*Re*) and Capillary (*Ca*) numbers, were evaluated to support this work. Eötvös (*Eö*) number (also known as Bond number, *Bo*) is defined according to Eq. 4.12 (AKBAR *et al.*, 2003):

$$Eö = \frac{\text{buoyancy}}{\text{surface tension}} = \frac{\Delta\rho g W^2}{\sigma} \tag{4.12}$$

In this work, *Eö* = 0.05 for the *phylic* and *phobic* cases. According to Shao *et al*. (2009), the *Eö* number can be used as a criterion for transition from macroscale to microscale flow indicating the relative importance of gravity and surface tension. Different criteria can be found in the literature for this transition: *Eö* <0.84 (BRETHERTON, 1961), <0.88 (SUO and GRIFFITH, 1964) and $<(2\pi)^2 \approx 39.5$ (BRAUNER and MARON, 1992). Therefore, the gravitational force can be adequately neglected in this work without significant impact on the flow pattern.

In all cases the Reynolds number, defined according to Eq. 4.13 (AKBAR *et al.*, 2003), indicated laminar flow conditions.

$$\mathrm{Re}_{(L,G)S} = \frac{\text{inertia}}{\text{viscous forces}} = \frac{j_{(L,G)S} W}{\upsilon_{(L,G)}} \tag{4.13}$$

According to Gad-el-Hak (2010), a wide range of critical *Re* for microchannel flow has been reported in the literature (from 200 to slightly

lower than the macroscale threshold). However, recent works have shown critical *Re* for microchannels consistent with the macroscale criterion, e.g., Re_c = 1,800 to 2,200 for rectangular cross sections (GAD-EL-HAK, 2010). In this work, *Re* = ~115 and ~3.0 for the liquid and gas phases, respectively, for both the *phylic* and *phobic* cases.

Finally, the *Ca* number can be evaluated according to Eq. 4.14 (GUPTA *et al*., 2009):

$$Ca = \frac{\text{viscous forces}}{\text{surface tension}} = \frac{\mu_L \left(j_{L,S} + j_{G,S} \right)}{\sigma} \tag{4.14}$$

In this work, *Ca* = 0.0036 indicating predominance of the surface tension forces over the viscous forces acting at the gas-liquid interface.

Thus, the cases studied are surface tension dominated under laminar flow. Moreover, gravity effect can be conveniently neglected in the simulations. In this scenario the importance of the wall wettability is maximized, enlarging its potential influence on the flow pattern developed in the device.

4.3.2 Mesh refinement study

Three different grid refinement levels were evaluated based on the structured mesh described in section 4.2.2. The *phylic* case was taken as reference due to the need of proper resolution of the thin liquid film that develops between the microchannel walls and the gas cavities elucidated elsewhere (GUPTA *et al*., 2009). The final mesh consisted of 1.4×10^5 (1.2×10^5), 6.1×10^4 (5.7×10^4) and 2.8×10^4 (2.7×10^4) elements for grids 1, 2 and 3, respectively, considering the *phylic* (*phobic*) case. Figure 4.2(a, b) presents the contours of absolute difference of liquid volume fraction in a unitary cell obtained in the *phylic* case for different mesh refinements.

In Figure 4.2a the liquid volume fraction obtained with grids 1 and 3 are compared. A significant deformation of the cavity shape can be noticed. Moreover, the liquid film between the microchannel walls and the gas cavity was not properly captured. On the other hand, Figure 4.2b shows the absolute difference of liquid volume fraction obtained when grids 1 and 2 are taken into account. Minimal difference can be observed and the liquid film was captured with both meshes. In Figure 4.2c these observations are supported showing the pressure profiles obtained at the mid-line of the domain for the three grids considered. Clearly the pressure

profiles obtained with grids 1 and 2 are very similar, while grid 3 resulted in a different behavior and was discarded.

Nevertheless, despite the similarity between the results obtained with grids 1 and 2, it was found that during the simulations the liquid film was resolved by only 1 grid cell at some instants, while grid 1 was able to maintain a layer of 3-4 grid cells across this film during the entire simulation. Therefore, given the importance of proper modeling of this phenomenon, grid 1 was adopted. The same mesh was used for the *phylic* and *phobic* cases for coherence. Figure 4.2(d. e) shows the liquid film formed above and below the gas cavity, respectively, when *phylic* case is simulated with grid 1.

Figure 4.2: Mesh refinement study: (a) contours of absolute difference of liquid volume fraction around a single cavity when grids 1 and 3 are compared (arrows highlight poor resolution at the microchannel walls); (b) contours of absolute difference of liquid volume fraction around a single cavity when grids 1 and 2 are compared; (c) pressure profile across a single cavity for different mesh refinements; (d) overview of the liquid film resolution between the top of the cavity and microchannel wall; (e) overview of the liquid film resolution between the bottom of the cavity and microchannel wall. The mesh consisted of 1.4×10^5 (1.2×10^5), 6.1×10^4 (5.7×10^4) and 2.8×10^4 (2.7×10^4) elements for grids 1, 2 and 3, respectively, considering the *phylic* (*phobic*) case.

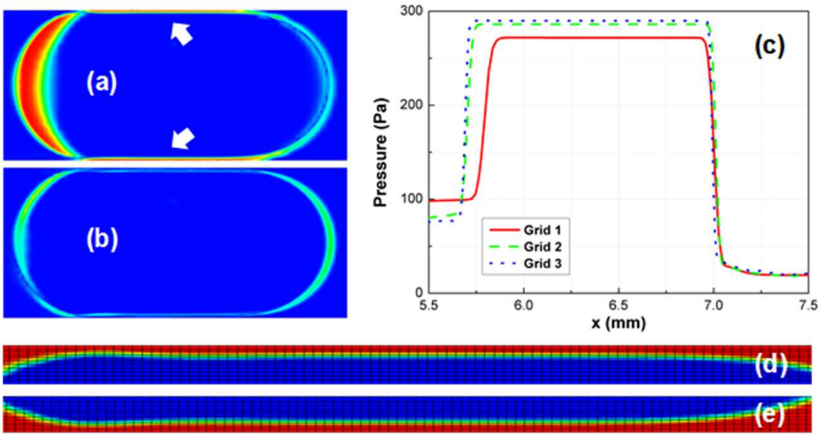

4.3.3 Analysis of the hydrophilic microchannel

According to the experimental observations of Choi *et al.* (2011), the flow pattern in case *phylic* ($\theta_w = 25°$) was characterized by intermittent

gas-liquid propagation through the main axis (*x*-coordinates). Particularly, the *elongated bubble* (also known as *Taylor* or *slug*) flow was reported for the case herein studied (see Figure 4.3a) (CHOI *et al.*, 2011).

A time-averaging procedure was carried out to evaluate the statistical steady state of the system studied, as recommended by Milioli and Milioli (2010). Time-averaged velocity profiles, obtained at the mid-line crossing the main channel in the *phylic* case, were used as reference. These profiles were taken after the completion of the first residence time and were evaluated at time intervals of Δt = 0.02375 s (corresponding to approximately half of the residence time of the *phylic* case). If the time-averaging is taken from the start, the simulation will always appears to converge if allowed infinite time, but it will only asymptotically approach the true time-averaged steady state value.

Figure 4.3: Isothermal gas-liquid flow patterns developed (a) in the hydrophilic (θ_w = 25°) microchannel and in the (b) hydrophobic (θ_w = 105°) microchannel used as reference (experimental data). Adapted from Choi *et al.* (2011).

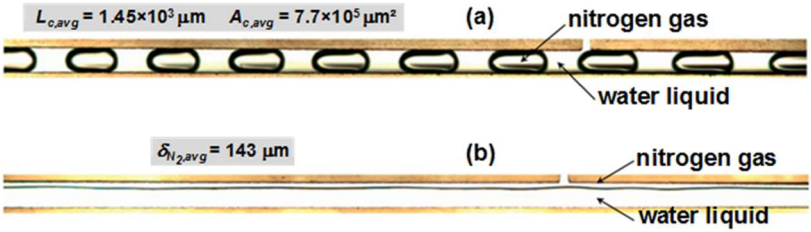

Figure 4.4 presents the time-averaged velocity profiles obtained for the *phylic* case. Although there was a variation between the profiles obtained in the first and second time intervals, there was almost a superposition of the profiles obtained in the first and third time intervals. This difference is due to the intermittent behavior of the flow herein studied. However, in all cases the mean velocity along the main axis mid-line was 365 mm·s^{-1} (0.365 m·s^{-1}). Therefore, the system promptly reached the statistical steady state.

The instantaneous velocity profile along the main axis mid-line (taken at the end of the third time-averaging interval) is also presented in Figure 4.4. The velocity at the cavity nose was approximately 265 mm·s^{-1} (0.265 m·s^{-1}). This value is close to the theoretical steady state cavity velocity in horizontal microchannels ($= \boldsymbol{j_{G,S}/\varepsilon_G}$) (GUPTA *et al.*, 2009),

calculated as 260 mm·s^{-1} (0.26 m·s^{-1}). Thus, the flow can be assumed as fully developed (GUPTA *et al*., 2009).

In fact, the gas cavities formed at the mixing region are subjected to a complex topological change but promptly stabilize, acquiring a form that is maintained as it travels along the microchannel. The cavity area (and length) remains constant during its passage along the channel. These observations support the assumption of a reduced domain for the modeling, allowing reduced computational cost while maintaining the main features of the experimental reference.

Figure 4.4: Time-averaged and instantaneous velocity profiles obtained at the mid-line of the main axis of the hydrophilic microchannel (*phylic* case). Each averaging procedure was carried out for the interval $\Delta t = 0.02375$ s after the completion of the first residence time. The instantaneous profile was obtained at the end of the third averaging procedure.

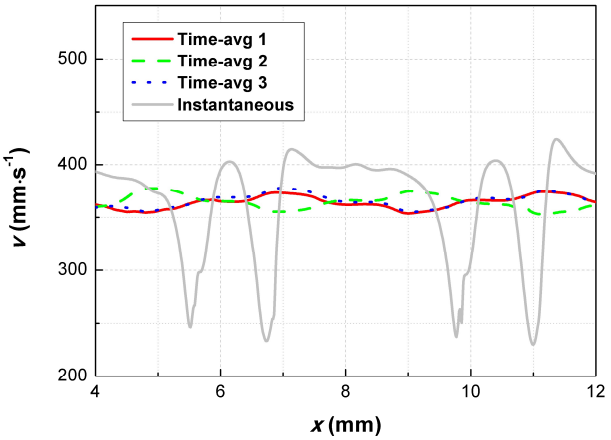

Figure 4.5a presents the two-dimensional flow pattern obtained numerically for the case *phylic*. The numerical simulation was able to capture the flow pattern corresponding to the scenario experimentally investigated. Moreover, Figure 4.5b highlights the vectors of the velocity field in a single gas cavity. Clearly, spurious currents were minimized in the simulations presented herein. Also, it should be noted that the liquid film developed between the microchannel walls and the gas cavities, whose importance is discussed elsewhere (GUPTA *et al*., 2009), was conveniently captured (with a resolution of 3-4 grid cells).

When considering the correlation proposed by Choi *et al.* (2011) for the calculation of the individual cavity pressure drop (ΔP_C) with the

parameter $C_1 = 1.14$, the value $\Delta P_C = 38$ Pa is obtained. On the other hand, considering $C_1 = 1.2$ the value of ΔP_C is 41 Pa. In the CFD simulations the predicted ΔP_C was c.a. 48 Pa. Therefore, the relative deviation of the numerically predicted value of individual cavity pressure drop and those obtained from the correlation of Choi *et al.* (2011) was 25% and 18%, when considering C_1 equal to 1.14 and 1.2, respectively. Figure 4.6 presents the pressure profile obtained at the main axis mid-line.

Figure 4.5: Taylor flow developed in the hydrophilic microchannel (*phylic* case): (a) contours of liquid volume fraction and (b) vectors of the velocity field in a single cavity.

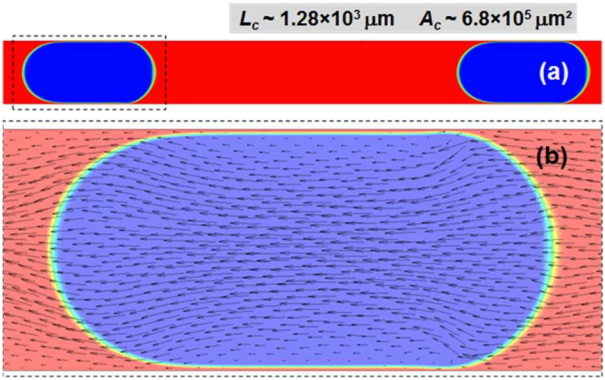

The numerically obtained maximum cavity length, measured at the mid-line of the microchannel through ImageJ software, was $L_C = 1.28\times10^3$ µm. Using the same procedure, the average cavity length of the experimental reference was $L_C = 1.45\times10^3$ µm, resulting in a deviation of 11.7%.

Additionally, the correlation of Qian and Lawal (2006) for the calculation of the cavity length in microchannels, enunciated according to Eq. 4.15, yielded an average length of 1,229 µm. The average cavity length predicted by the numerical simulations deviated from this value by 4.1%. The correlation of Qian and Lawal (2006) was obtained in channels with width 1 mm or less and considers that $0.09 < \varepsilon_G < 0.91$, $15 < Re < 1{,}500$ and $2.78\times10^{-4} < Ca < 0.01$, which satisfy the conditions of the case *phylic*, where $\varepsilon_G = 0.27$, $Re = 160$ and $Ca = 0.0036$. Interestingly, the authors reported a deviation between the correlation and their simulated data of approximately 10%.

$$L_C = W\left[1.637\varepsilon_G^{0.107}\left(1-\varepsilon_G\right)^{-1.05}\mathrm{Re}^{-0.075}\,\mathrm{Ca}^{-0.0687}\right], \tag{4.15}$$

where L_C is the cavity length, W is the microchannel width, $\boldsymbol{\varepsilon_G = j_G/(j_G + j_L)}$ is the gas holdup, *Re* is the Reynolds number (defined by Qian and Lawal (2006) as $\boldsymbol{Re}$ $\boldsymbol{[\rho_L(j_G + j_L)W/\mu_L]}$) and $\boldsymbol{Ca = [\mu_L(j_G + j_L)/\sigma]}$ is the capillary number.

Figure 4.6: Pressure profile obtained at the mid-line of the main axis of the hydrophilic microchannel (*phylic* case). Two consecutive cavities are highlighted.

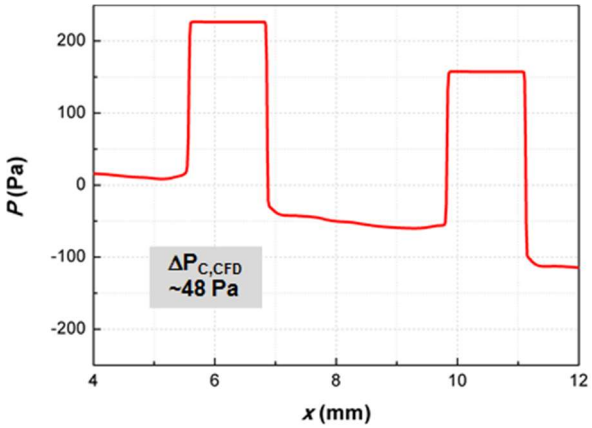

On the other hand, the correlation of Sobieszuk *et al.* (2010), defined according to Eq. 4.16, provided a cavity length of 1,120 µm, which is a value 14.2% lower than that predicted by the numerical simulation.

$$L_C = W\left[1.302\varepsilon_G^{0.073}\left(1-\varepsilon_G\right)^{-1.01}\mathrm{Re}^{-0.098}\,\mathrm{Ca}^{-0.108}\right] \tag{4.16}$$

Sobieszuk *et al.* (2010) reported that the proposed correlation is valid for $0.1 < We < 26$, $0.02\ \mathrm{m{\cdot}s^{-1}} < j_G$ (superficial) $< 1.2\ \mathrm{m{\cdot}s^{-1}}$, $0.004\ \mathrm{m{\cdot}s^{-1}} < j_L$ (superficial) $< 0.7\ \mathrm{m{\cdot}s^{-1}}$ and $0.06 < \varepsilon_G < 0.85$, which is satisfied in case *phylic*, where $We = 0.58$ (calculated as We $[(j_G + j_L)^2 W\rho_L/\sigma]$), $j_G = 0.07\ \mathrm{m{\cdot}s^{-1}}$, $j_L = 0.19\ \mathrm{m{\cdot}s^{-1}}$ and $\varepsilon_G = 0.27$.

Finally, the superficial area of the cavities obtained numerically was approximately 6.8×10^5 µm^2 (0.68 mm^2), while the equivalent average value measured from the experimental reference was 7.7×10^5 µm^2 (0.77

mm^2). Therefore, a deviation of 12% was obtained when comparing the superficial area of the simulated and experimental cavities.

4.3.4 Analysis of the hydrophobic microchannel

Similarly, the hydrophobic microchannel (*phobic* case, θ_w = 105°) was subjected to a time-averaging procedure for the evaluation of the statistical steady state. Time-averaged profiles were taken at three lines perpendicular to the main axis (located at 3.0, 7.5 and 12 mm from the liquid inlet) after reaching stable flow condition (t = 0.025 s). The profiles were evaluated at time intervals of Δt = 0.02375 s (for coherence with the analysis performed in the *phylic* case). Figure 4.7 presents the time-averaged velocity profiles obtained at the three control lines for the different time intervals considered. The statistical steady state was also promptly reached in the *phobic* case.

Figure 4.8a presents contours of liquid volume fraction (liquid = red, gas = blue) in the hydrophobic microchannel. The computational model allowed the prediction of a stratified gas-liquid flow pattern, as experimentally observed by Choi *et al.* (2011) (see Figure 4.3b for reference).

In the experimental data obtained by Choi *et al.* (2011) (Figure 4.3b) an average gas film thickness of δ = 143 μm was obtained. In the simulations herein reported an average gas film thickness of δ = 142 μm was obtained. Therefore, there was excellent agreement between the experimental and the simulated flow morphologies (error of 0.7%).

Figure 4.8b presents the vectors of the velocity field at the center of the microchannel. Again, it can be noticed that spurious currents were minimized in this work. Additionally, Figure 4.8c shows details of the mesh used in the *phobic* case simulations (same used in the *phylic* case). It should be emphasized that the same feeding conditions were imposed to the *phylic* and *phobic* cases ($j_{in,G}$ = 0.07 m·s^{-1} and $j_{in,L}$ = 0.19 m·s^{-1}). Apart of the slight difference in the microchannel width (W = 617 μm and W = 608 μm in the *phylic* and *phobic* cases, respectively), to comply with the geometrical features experimentally evaluated, the only parameter varied in the simulations was the wall contact angle (θ_w). In a surface tension dominated flow the wall wettability has profound effect on the gas-liquid flow morphology observed. Changing the wall condition from hydrophilic to hydrophobic resulted in a shift from Taylor flow to stratified flow pattern. Thus, the interfacial area available for heat and mass transfer and chemical reactions in these devices was affected,

inducing a significant impact of the wall wettability on the system performance.

Figure 4.7: Time-averaged velocity profiles obtained at three lines perpendicular to the main axis of the hydrophobic microchannel (*phobic* case) located at 3.0, 7.5 and 12 mm from the liquid inlet. Each averaging procedure was carried out for the interval Δt = 0.02375 s after the completion of the first residence time and flow stabilization.

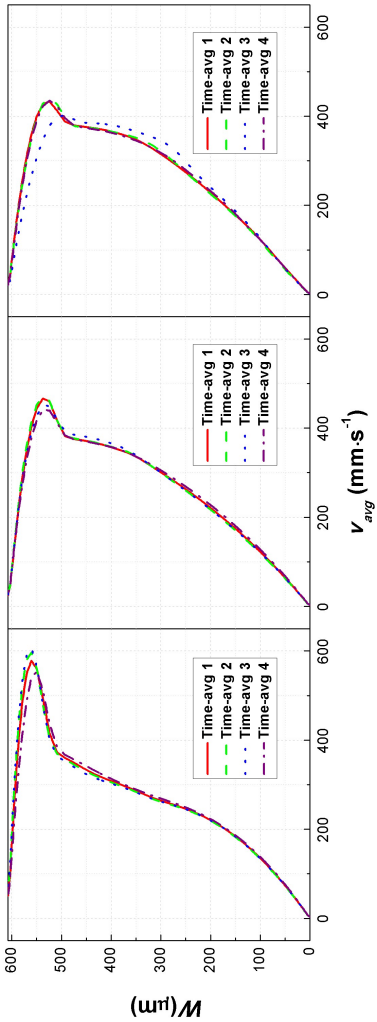

Figure 4.8: Stratified flow developed in the hydrophobic microchannel (*phobic* case): (a) contours of liquid volume fraction; (b) vectors of the velocity field at the center of the computational domain and (c) mesh details.

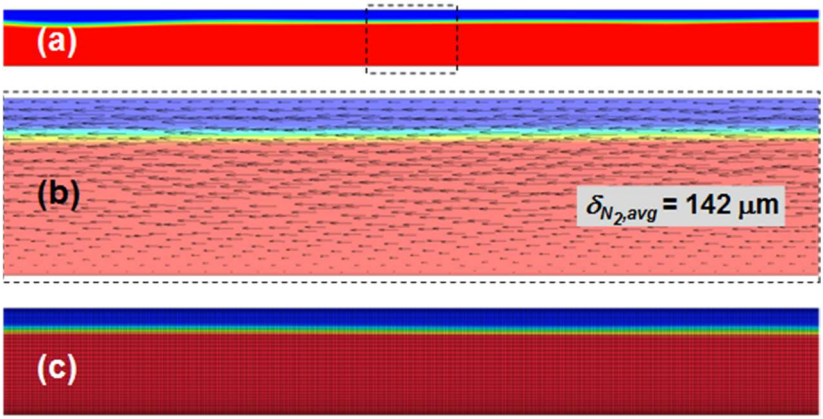

4.3.5 Complementary study – sensitivity of varying θ_w suppressing external convection

Figure 4.9 presents a sensitivity analysis of the effect of varying the wall contact angle on the interface evolution predicted by the CFD simulations.

The initial interface at rest (t = 0 s) (Figure 4.9a) was allowed to evolve during Δt = 1 ms considering hydrophilic (θ_w = 25°) and hydrophobic (θ_w = 105°) walls at the bottom of the domain (Figures 4.9b and 4.9c, respectively). It should be emphasized that at the beginning of the simulation the velocity in the entire domain was null and no convective contribution was assigned in neither boundary of the domain.

Clearly, the gas-liquid interface assumed different morphologies when changing the wall wettability conditions. At the end of the simulations (t = 1 ms) a stabilized interface was reached, approaching the hydrodynamic equilibrium asymptotically.

In this study, the interface was allowed to evolve exclusively due to the surface tension forces. Thus, it is demonstrated that completely different morphologies can be obtained at the gas-liquid interface assigning different contact angles at the walls, which consequently affects the gas-liquid flow patterns in surface tension dominated flows, as in the case of microfluidic devices.

Figure 4.9: Gas-liquid interface evolution as a function of the wall wettability condition: (a) initial condition when the interface is at rest (t = 0 s); (b) interface evolution after Δt = 1 ms considering hydrophilic wall (θ_w = 25°); (c) interface evolution after Δt = 1 ms considering hydrophobic wall (θ_w = 105°).

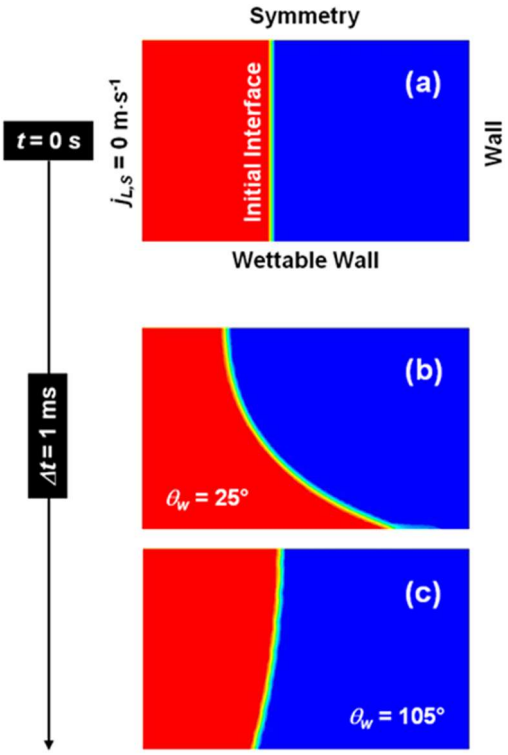

4.4. CONCLUSIONS

Microchannel technology has been pointed out as a promising route for process intensification and design of compact equipment. Frequently, multiphase flow takes place in these devices and the predictability of the flow pattern plays a major role for the proper project.

This study highlighted that CFD can be applied to the investigation of isothermal gas-liquid flow patterns in microchannels with different wettability conditions. In particular, the Taylor and the stratified flow patterns were observed in hydrophilic (θ_w = 25°) and hydrophobic (θ_w = 105°) rectangular microchannels subjected to the same feeding

conditions and with similar geometry. Only the contact angle specified at the wall was significantly changed in the problem setup.

The numerical studies were based on the experimental setup investigated by Choi *et al.* (2011) and agreed reasonably well with the data presented by these authors. The numerically predicted pressure drop per cavity showed good agreement with the ΔP_C obtained from the correlation of Choi *et al.* (2011). In addition, good agreement was obtained between the numerically predicted maximum length of the cavities and the values obtained from the work of Choi *et al.* (2011) and the correlations of Qian and Lawal (2006) and Sobieszuk *et al.* (2010). Furthermore, good agreement was obtained between the predicted surface area of the cavities and the data obtained from Choi *et al.* (2011). Finally, excellent agreement was obtained between the numerical and the experimental gas layer thickness obtained in the stratified flow pattern.

In summary, in surface tension dominated flows, as in the case of gas-liquid flows in microchannels under the conditions herein studied, a variation in the wall wettability has significant impact on the flow pattern developed. Thus, it affects the interfacial area available for heat and mass transfer and for chemical reactions in these devices. CFD can be used to acquire preliminary information about the flow pattern expected in microfluidic devices subjected to superficial treatment.

4.5 IMPRESSIONS AND PERSPECTIVES

During the development of the research reported in this chapter some difficulties were observed. In particular, the main problem was to obtain a mesh able to adequately capture, with consistent computational cost, the liquid film formed between the gas cavity and the solid wall in the case of a hydrophilic microchannel. The model was greatly modified along the development of the research reported herein.

Initially, a three-dimensional geometry reproducing exactly the same dimensions of the experimental platform used as reference was considered. A structured mesh was constructed and, in a global perspective, the flow patterns obtained experimentally were reproduced with the computational model. However, it was found that this configuration was not able to capture the liquid film formed between the gas cavity and the solid wall in the case of hydrophilic microchannel. A much finer mesh should be used. However, even with the original discretization, a long time was needed to simulate the system (typically 2.5 months). Therefore, using an adequately fine mesh sufficient to capture the liquid film in the three-dimensional geometry considering the

same dimensions of the experimental reference was unfeasible from the point of view of the computational cost associated to this. Therefore, several tests were performed aiming to obtain a representative domain able to allow adequate representation of the phenomenon considering all features of the experimental reference. In addition, a detailed mesh independence study was conducted, aiming to reach an optimal condition in terms of computational cost and adequate modeling of the liquid film formed in Taylor flow. Moreover, some effort was necessary to minimize spurious currents typically encountered in surface tension dominated flow. The final configuration of the geometry, mesh and solution method allowed the simulation of each case in a few days.

The computational model presented and discussed in this chapter could be used in further studies aiming to investigate the effect of varying the wall wettability at discrete values through a large window. Moreover, the effect of varying fluid pairs and geometrical configurations (e.g., the angle formed between the feeding channels at the mixing region) should be evaluated. Additionally, a comprehensive investigation of the effect of varying the feed velocity of each phase on the flow pattern developed in microfluidic devices should be considered in further contributions based on the numerical workflow presented herein. Finally, non-isothermal multiphase flow could be considered. In this case, a deep investigation considering mass and heat transfer, phase change and, eventually, chemical reactions, should be carried out.

5. THE ESSENCE (WHAT SHOULD BE KEPT IN MIND?) AND CONCLUDING REMARKS

Like any thesis, this document represents only a water molecule in the vast ocean of knowledge. It surely does not intend to be a watershed, but a little contribution to the advance of Engineering Science.

Basically, this thesis aimed to provide contributions to the field of photochemical microfluidics. Some gaps not answered in the literature so far in this field were covered in this document. As stated in Section 1.1, these questions are:

- What is the behavior of microfluidic devices applied to the intensification of photocatalytic processes when considering composite photocatalyst attached on the active walls? When using a composite of TiO_2 and graphene, in particular, how it performs when compared to systems with pristine TiO_2 used as photocatalyst?
- Is it possible to investigate theoretically the behavior of microfluidic systems applied to photocatalytic processes based on fundamental physics of semiconductors? Would it be possible to successfully computationally model the coupled phenomena, i.e., radiation distribution, fluid flow, mass transport and chemical reactions, that occur in microchannel reactors (providing an estimative of the reactor performance, globally and locally)?
- Would it be possible to find an explicit function of optimal photocatalyst film thickness to be deposited on the walls of microfluidic devices considering relevant variables that govern the system dynamics?
- Is it possible to computationally model the effect of the wall wettability on the flow pattern developed in microchannels so that one could predict the behavior of different washcoats on possible multiphase flow applications in photocatalytic processes carried out in microfluidic devices?

It should be analyzed at this point if this thesis was able to properly answer such questions and discuss implications derived from the work reported herein.

Chapter 2 was based on the article entitled “Intensification of photocatalytic pollutant abatement in microchannel reactor using TiO_2 and TiO_2-graphene”, by Natan Padoin, Luísa Andrade, Joana Ângelo, Adélio Mendes, Regina de Fátima Peralta Muniz Moreira and Cíntia Soares, published in *AIChE Journal* (Volume 62, Number 8, August 2016, Pages 2794–2802).

There is a growing interest in the application of microfluidics to the intensification of photocatalytic processes and several works have been published in this direction. While most of them use pristine TiO_2 as photocatalyst, recent works have investigated the use of composite photocatalysts for flow chemistry in microfluidic devices. Nevertheless, up to the date of publication of the article presented in Chapter 2, there was no contribution reported in the literature regarding the use of TiO_2-graphene as photocatalyst immobilized on the inner walls of microchannel reactors to the best of our knowledge.

Graphene is an emerging material. Its outstanding properties have been largely discussed, e.g., high surface area, good electrical conductivity, etc. Composite photocatalysts of TiO_2-graphene have been already tested in batch reactors and exhibited good performance. In these systems, the catalyst is usually dispersed, under vigorous agitation. Its application in microfluidic devices, however, requires a proper methodology for immobilization on the internal channel walls. In this work, for the first time, a procedure for immobilization of TiO_2-GR on the walls of microchannels was reported.

The performance of microfluidic chips containing TiO_2 and TiO_2-GR for de decolourization of methylene blue, under identical conditions, was compared and it was found that at the steady state both systems tend to perform similarly. Although the chemical kinetics was modified, i.e., the system containing TiO_2-GR exhibited a higher initial decolourization rate compared to pristine TiO_2, the thermodynamics was not.

The use of composite photocatalysts deposited on the walls of microfluidic devices is advantageous, since the intrinsic properties of the active material can be enhanced this way, leading to higher reaction rates. Moreover, one can even use this configuration to harvest sunlight, which is not possible when pristine TiO_2 is used. It should be highlighted that other composite photocatalysts apart from TiO_2-graphene also exhibit this property and have been tested in microfluidic devices, but this work was indeed the first one to use graphene combined with TiO_2 as photoactive material in a microfluidic chip. Research in this direction is important since it has been proposed the development, in the near future, of compact

modular reactors based on microchannel technology to be used in different scenarios.

The effective application of microfluidics for the intensification of photocatalytic processes in real scale passes through efficient scale-out methodologies able to get the most of each *unitary cell*, i.e., each individual microchannel. This can be achieved only through modeling of the system dynamics rigorously. In this regard, the use of fundamental physical concepts, with as minimal approximation as possible, is essential. An effective model should consider the radiation distribution in the system, preferably taking into account each photocatalyst film arrange individually, the fluid flow through the microchannels, the mass transport and the chemical reactions.

Some works have been published aiming to computationally model reactive flow in microfluidic systems. Few of them, however, deal with photocatalytic processes and do not consider the coupling of several phenomena occurring in these devices.

In microchannel reactors, frequently a combination of irradiation mechanisms, i.e., backside illumination and front-side illumination, is encountered. This arises from the fact that usually the light source is positioned outside the flow channel containing the photocatalyst deposited on the inner walls. Photons reach the first photocatalyst layer with a backside illumination mechanism and a fraction of the incident beam is transmitted reaching the next photocatalyst layer with a front-side illumination mechanism. A condition in which only front-side illumination occurs is reached if the light source is positioned inside the flow channel. While this is feasible in macro-sized equipment, it remains unpractical in microchannel reactors. This topic is, indeed, an interesting research theme.

Moreover, when considering real-scale equipment, several light arranges can be set up. In this regard, an external or internal numbering-up strategy may be used. When external numbering up is considered, the light source is positioned outside the array of capillary tubes. On the other hand, when the lamp, or usually a fewer unities of it, is positioned inside the equipment, an internal numbering up strategy is reached.

Internal numbering-up strategies usually lead to more efficient operations, but the design and optimization of this equipment is more complex. Only through rigorous modeling approaches one can properly design this equipment.

This thesis contributed in this direction, proposing a methodology for comprehensive computational modeling of photocatalytic processes in microfluidic devices considering in its

development concepts of the fundamental physics of semiconductors and the coupling of relevant phenomena involved in these systems. The approach presented herein could be applied for the design and optimization of real-scale modular reactors based on microchannel technology, where the photocatalytic process is considerably intensified. With a structured model, as the one presented, different configurations could be readily tested and optimized.

During the development of the research reported in this document, it was noticed how important is a proper design of the photocatalytic film for the global performance of the system. It is unfruitful to optimize the flow channel, the illumination arrange and, in the case of modular equipment, the bunch of microcapillaries if the photocatalytic film attached to the walls is not well designed. As aforementioned, the photocatalytic film is usually subjected to two possible illumination mechanisms: backside illumination (BSI) or front-side illumination (FSI). In microfluidic devices, a complex interaction of both mechanisms, in a global sense, is usually encountered.

Based on this scenario, a theoretical investigation about the effect of the incident irradiation, the apparent first-order reaction constant, the effective diffusivity and the absorption coefficient on the optimal thickness of photocatalyst immobilized on the walls of microfluidic devices was carried out and reported in Chapter 3. It has been found that the optimal film thickness depends only on the catalyst parameters and its interaction with the operational conditions of the system. Variables affecting the fluid phase do not contribute for the establishment of the optimal location of the film thickness on the multiparametric space evaluated.

Finally, it is worthy to mention that microfluidic systems are highly dependent on the conditions imposed at the walls, due to the high surface-to-volume ratio. According to Bejan (2016) it is just this property that ensures a evolutive advantage to micro-sized systems when compared to macro-sized equipment. Microfluidic systems present a higher density of functionality or a higher density of flow per unit of volume (BEJAN, 2016).

Given this scenario, one can state that bulk contribution is greatly diminished in microchannel reactors when compared with equivalent macroscopic systems. In microreactors, the fluid-solid interface plays a major role on the overall performance. Thus, a proper catalyst deposition is necessary in the case of heterogeneous reactive flow. But one cannot forget to look at how the wall condition may affect the flow developed in the channel.

When monophasic flow is considered, the wall contribution is concentrated on the friction due to imperfections that influence on the shear stress, considering that usually laminar flow is established in microchannels. However, in a more generic case, multiphase flow can be developed in microfluidic devices, e.g., gas-liquid flow. This condition could be achieved, for instance, if air (or oxygen) is injected along with the liquid phase in the microchannels to enhance the photocatalytic reaction rate, which would lead to an even higher level of intensification. The same condition would be achieved if ozone is injected along with the liquid phase.

If a gas-liquid flow develops in a microchannel, the wall will influence on the flow properties due to the surface tension forces. In this condition, the wall wettability (i.e., hydrophobicity or hydrophilicity) may significantly alter the flow pattern developed in the channel. Thus, different morphologies at the gas-liquid interface may be expected, which will impact the overall system performance affecting the interfacial area available for momentum, heat and mass transfer.

While there are experimental contributions in the literature showing the effect of varying the wall wettability on the gas-liquid flow developed in microchannels (see the work of Choi *et al.* (2011) for reference), there was no systematic work published so far dealing with computational modeling of the impact of the wall contact angle on gas-liquid flow morphology in microfluidic platforms. In this thesis, particularly in Chapter 4, this gap was approached.

It has been shown in this document that it is possible to numerically simulate the flow patterns developed under different wall wettability. In particular, extreme conditions of highly hydrophilic and highly hydrophobic walls were investigated and it was demonstrated that it is possible to computationally reproduce, with significant accuracy, the results obtained experimentally by Choi *et al.* (2011).

This workflow is important for the design and optimization of real-scale modular photocatalytic reactors in which multiphase flow is taken into account. One could, then, know *a priori* which flow regime is expected depending on the washcoat properties and adjust the inlet configuration, for instance, to get the higher performance from the system (maximizing mass transfer and the reaction rate and minimizing the pressure drop, for instance). Different washcoats apart of pristine TiO_2, such as composite photocatalysts including TiO_2-graphene evaluated in this thesis, may exhibit significantly different wettability, which justifies the study carried out herein. Moreover, it should be emphasized that several aspects related to theoretical investigation of multiphase flow in

microchannels under different wettability conditions are still not covered in the literature and, thus, works derived from the research reported in Chapter 4 of this thesis are under way in our research group to be published soon.

Therefore, based on the previous discussion, the following thesis arises from the work conducted herein:

Carbon-based composite photocatalysts, specifically a composite of TiO_2 and graphene, can be attached on the walls of microfluidic devices applied to photocatalytic processes. However, even though the chemical kinetics is influenced by the composition with graphene, the thermodynamics is not and essentially the same steady state is reached when compared with systems containing pristine TiO_2. The dynamics of such systems can be successfully computationally modeled based on fundamental physics of semiconductors and considering the coupling of radiation distribution, fluid flow, mass transport and chemical reaction. In addition, it is possible to find an explicit correlation that takes into account the photocatalyst film thickness as a function of relevant operational variables and parameters (incident irradiation, apparent first-order reaction constant, effective diffusivity and absorption coefficient), which can be used, in combination with the general modeling workflow, for scale-out studies aiming to design real-scale compact equipment. Finally, it would be possible to computationally model the effect of the wall wettability in microfluidic devices, which can be used as a source of a priori information on the flow pattern the develops in microchannels depending on the washcoat properties when multiphase flow is considered.

Some final remarks should be added. As already mentioned throughout this section, other works have been carried out in our group aiming to investigate experimentally and theoretically microfluidic systems. Moreover, additional studies derived from this thesis are under way, particularly a phenomenological investigation about the size effect on the performance of reactive systems, using fundamental concepts of transport phenomena, thermodynamics and chemical reaction engineering, and the design of a compact modular reactor that will be built upon concepts of microchannel technology for application in photocatalytic processes.

By the way, a preliminary concept of a compact modular reactor that has been investigated by our group was submitted as a proposal to the 1st Elsvier Green and Sustainable Chemistry Challenge, in 2015. From a total of almost 500 proposals submitted globally, our work was selected to the semifinal round in a group of 53 proposals.

6. REFERENCES

ABADIE, T.; AUBIN, J.; LEGENDRE, D.; XUEREB, C. **Hydrodynamics of gas-liquid Taylor flow in rectangular microchannels**. Microfluid Nanofluid, v. 12, n. 1, p. 355-369, 2012.

AKBAR, M. K.; PLUMMER, D. A.; GHIAASIAAN, S. M. **On gas-liquid two-phase flow regimes in microchannels**. International Journal of Multiphase Flow, v. 29, n. 1, p. 855-865, 2003.

ÂNGELO, J.; ANDRADE, L.; MADEIRA, L. M.; MENDES, A. **Na overview of photocatalysis phenomena applied to NOx abatement**. Journal of Environmental Management, v. 129, n. 1, p. 522-539, 2013.

ARAN, H. C.; SALAMON, D.; RIJNAARTS, T.; MUL, G.; WESSLING, M.; LAMMERTINK, R. G. H. **Porous photocatalytic membrane microreactor (P2M2): A new reactor concept for photochemistry**. Journal of Photochemistry and Photobiology A: Chemistry, v. 225, n. 1, p. 36-41, 2011.

BEJAN, A. **The physics of life: The evolution of everything.** St. Martin's Press: New York, 2016.

BEJAN, A.; LORENTE, S. **Constructal law of design and evolution: Physics, biology, technology, and society**. Journal of Applied Physics, v. 113, n. 1, p. 151301-1 - 151301-20, 2013.

BOYJOO, Y.; ANG, M.; PAREEK, V. **Some aspects of photocatalytic reactor modeling using computational fluid dynamics**. Chemical Engineering Science, v. 101, n. 1, 764-784, 2013.

BRACKBILL, J. U.; KOTHE, D. B.; ZEMACH, C. **A continuum method for modeling surface tension**. Journal of Computational Physics, v. 100, n. 1, p. 335-354, 1992.

BRAUNER, N.; MARON, D. M. **Identification of the range of 'small diameters' conduits, regarding two-phase flow pattern transitions**. International Communications in Heat and Mass Trasnfer, v. 19, n. 1, p. 29-39, 1992.

BRETHERTON, F. P. **The motion of long bubbles in tubes**. Journal of Fluid Mechanics, v. 10, n. 1, p. 166-188, 1961.

CHARLES, G.; ROQUES-CARMES, T.; BECHEIKH, N.; FALK, L.; COMMENGE, J.- M.; CORBEL, S. **Determination of kinetic constants of a photocatalytic reaction in micro-channel reactors in the presence of mass-transfer limitation and axial dispersion**. Journal of Photochemistry and Photobiology A: Chemistry, v. 223, n. 2-3, p. 202-211, 2011.

CHARLES, G.; ROQUES-CARMES, T.; BECHEIKH, N.; FALK, L.; CORBEL, S. **Impact of the design and the materials of rectangular microchannel reactors on the photocatalytic decomposition of organic pollutant**. Green Processing and Synthesis, v. 1, n. 4, p. 363–374, 2012.

CHEN, D.; LI, F.; RAY, A. K. **External and internal mass transfer effect on photocatalytic degradation**. Catalysis Today, v. 66, n. 2, p. 475-485, 2001.

CHOI, C.; YU, D. I.; KIM, M. **Surface wettability effect on flow pattern and pressure drop in adiabatic two-phase flows in rectangular microchannels with T-junction mixer**. Experimental Thermal and Fluid Science, v. 35, n. 1, p. 1086-1096, 2011.

CHOI, W.; KO, J. Y.; PARK, H.; CHUNG, J. S. **Investigation on TiO_2-coated optical fibers for gas-phase photocatalytic oxidation of acetone**. Applied Catalysis B: Environmental, v. 31, n. 3, p. 209-220, 2001.

CHUNG, P. M. Y.; KAWAJI, M. **The effect of channel diameter on adiabatic two-phase flow characteristics in microchannels**. International Journal of Multiphase Flow, v. 30, n. 1, p. 735-761, 2004.

CORBEL, S.; BECHEIKH, N.; ROQUES-CARMES, T.; ZAHRAA, O. **Mass transfer measurements and modeling in a microchannel photocatalytic reactor**. Chemical Engineering Research and Design, v. 92, n. 4, p. 657-662, 2014.

COYLE, E. E.; OELGEMOLLER, M. **Micro-photochemistry: photochemistry in microstructured reactors. The new**

photochemistry of the future? Photochemical & Photobiological Sciences, v. 7, n. 11, p. 1313-1322, 2008.

CUBAUD, T.; HO, C.- M. **Transport of bubbles in square microchannels**. Physics of Fluids, v. 16, n. 1, p. 4575-4585, 2004.

DAI, L.; CAI, W.; XIN, F. **Numerical study on bubble formation of a gas-liquid flow in a T-junction microchannel**. Chemical Engineering & Technology, v. 32, n. 1, p. 1984-1991, 2009.

DEAN, R. N.; SURGNIER, S.; PACK, J.; SANDERS, N.; REINER, P.; LONG, C. W.; FENNER, R.; FENNER, W. P. **Porous ceramic packing for a MEMS humidity sensor requiring environmental access**. IEEE Transactions on Components, Packaging and Manufacturing Technology, v. 1, n. 1, p. 428-435, 2011.

FLUENT, A. **15.0 Documentation**. Ansys Inc., 2013.

GAD-EL-HAK, M. **MEMS: Introduction and fundamentals**. CRC Press, 2010.

GAVRIILIDIS, A.; ANGELI, P.; CAO, E.; YEONG, K. K.; WAN, Y. S. S. **Techbology and applications of microengineered reactors**. Chemical Engineering Research and Design, v. 80, n. 1, p. 3-30, 2002.

GORGES, R.; MEYER, S.; KREISEL, G. **Photocatalysis in microreactors**. Journal of Photochemistry and Photobiology A: Chemistry, v. 167, n. 1, p. 95-99, 2004.

GUO, F.; CHEN, B. **Numerical study on Taylor bubble formation in a micro-channel T-junction using VOF method**. Microgravity Sci. Technol., v. 21, n. 1, p. 51-58, 2009.

GUPTA, R.; FLETCHER, D. F.; HAYNES, B. S. **On the CFD modelling of Taylor flow in microchannels**. Chemical Engineering Science, v. 64, n. 1, p. 2941-2950, 2009.

HARTMAN, R. L.; McMULLEN, J. P.; JENSEN, K .F. **Deciding whether to go with the flow: Evaluating the merits of flow reactors for synthesis**. Angewandte Chemie International Edition, v. 50, n. 1, p. 7502-7519, 2011.

HUMMERS, W. S.; OFFEMAN, R. E. **Preparation of graphitic oxide**. Journal of the American Chemical Society, v. 80, n. 6, p. 1339-1339, 1958.

JÄHNISCH, K.; HESSEL, V.; LÖWE, H.; BAERNS, M. **Chemistry in microstructured reactors**. Angewandte Chemie International Edition, v. 43, n. 4, p. 406-446, 2004.

KENIG, E. Y.; SU, Y.; LAUTENSCHLEGER, A.; CHASANIS, P.; GRÜNEWALD, M. **Micro-separation of fluid systems: A state-of-the-art review**. Separation and Purification Technology, v. 120, n. 1, p. 245-264, 2013.

KIM, K.; KIM, M.- J.; KIM, S.- I.; JANG, J.- H. **Towards visible light hydrogen generation: quantum dot-sensitization via efficient light harvesting of hybrid-TiO_2**. Scientific reports, v. 3, 2013.

LAM, K. F.; SORENSEN, E.; GAVRIILIDIS, A. **Review on gas-liquid separations in microchannel devices**. Chemical Engineering Research and Design, v. 91, n. 1, p. 1941-1953, 2013.

LING, C. M.; MOHAMED, A. R.; BHATIA, S. **Performance of photocatalytic reactors using immobilized TiO_2 film for the degradation of phenol and methylene blue dye present in water stream**. Chemosphere, v. 57, n. 7, p. 547-554, 2004.

MAGALHÃES, P.; ÂNGELO, J.; SOUSA, V. M.; NUNES, O. C.; ANDRADE, L.; MENDES, A. **Synthesis and assessment of a graphene-based composite photocatalyst**. Biochemical Engineering Journal, v. 104, n. 1, p. 20-26, 2015.

MATSUSHITA, Y.; OHBA, N.; KUMADA, S.; SAKEDA, K.; SUZUKI, T.; ICHIMURA, T. **Photocatalytic reactions in microreactors**. Chemical Engineering Journal, v. 135, n.1, p. S303-S308, 2008.

McCULLAGH, C.; ROBERTSON, P. K. J.; ADAMS, M.; POLLARD, P. M.; MOHAMMED, A. **Development of a slurry continuous flow reactor for photocatalytic treatment of industrial waste water**. Journal of Photochemistry and Photobiology A: Chemistry, v. 211, n. 1, p. 42-46, 2010.

MILIOLI, C. C.; MILIOLI, F. E. **On the accuracy of two-fluid model predictions for a particular gas-solid riser flow**. Applied Mathematical Modelling, v. 34, n. 1, p. 684-696, 2010.

MILLS, P.L.; QUIRAM, D.J.; RYLEY, J. F. **Microreactor technology and process miniaturization for catalytic reactions — A perspective on recent developments and emerging technologies**. Chemical Engineering Science, v. 62, n. 24, p. 6992-7010, 2007.

MILOZIC, N.; LUBEJ, M.; NOVAK, U.; ZNIDARSIC-PLAZL, P.; PLAZL, I. **Evaluation of diffusion coefficient determination using a microfluidic device**. Chemical and Biochemical Engineering Quarterly, v. 28, n. 2, p. 215-223, 2014.

NGUYEN-PHAN, T.- D.; PHAM, V. H.; SHIN, E. W.; *et al*. **The role of graphene oxide content on the adsorption-enhanced photocatalysis of titanium dioxide/graphene oxide composites**. Chemical Engineering Journal, v. 170, n. 1, p. 226-232, 2011.

NIELSEN, M. G.; IN, S. -I.; VESBORG, P. C. K.; PEDERSEN, T.; ALMTOFT, K. P.; ANDERSEN, I. H.; HANSEN, O.; CHORKENDORFF, I. **A generic model for photocatalytic activity as a function of catalyst thickness**. Journal of Catalysis, v. 289, n. 1, p. 62-72, 2012.

NOËL, T.; SU, Y.; HESSEL, V. **Beyond organimetallic flow chemistry: The principles behind the use of continuous-flow reactors for synthesis**. Springer Berlin Heidelberg, Berlin, 2015.

OFFEMAN, R.; HUMMERS, W. **Preparation of graphitic oxide**. J Am Chem Soc, v. 80, n. 1, p. 1339-1339, 1958.

OULD-MAME, S. M.; ZAHRAA, O.; BOUCHY, M. **Photocatalytic degradation of salicylic acid on fixed TiO_2 – kinetic studies**. International Journal of Photoenergy, v. 2, n. 1, p. 59-66, 2000.

QIAN, D.; LAWAL, A. **Numerical study on gas and liquid slugs for Taylor flow in a T-junction microchannel**. Chemical Engineering Science, v. 61, n. 1, p. 7609-7625, 2006.

RAMOS, B.; OOKAWARA, S.; MATSUSHITA, Y.; YOSHIKAWA, S. **Low-cost polymeric photocatalytic microreactors: Catalyst deposition and performance for phenol degradation**. Journal of Environmental Chemical Engineering, v. 3, n. 3, p. 1487-1494, 2014.

REIS, N. M.; LI PUMA, G. **A novel microfluidic approach for extremely fast and efficient photochemical transformations in fluoropolymer microcapillary films**. Chemical Communications, v. 51, n. 40, p. 8414-8417, 2015.

RUSSO, D.; SPASIANO, D.; VACCARO, M.; *et al*. **Direct photolysis of benzoylecgonine under UV irradiation at 254 nm in a continuous flow microcapillary array photoreactor**. Chemical Engineering Journal, v. 283, n. 1, 243-250, 2016.

SANTOS, R. M.; KAWAJI, M. **Numerical modeling and experimental investigation of gas-liquid slugs formation in a microchannel T-junction**. International Journal of Multiphase Flow, v. 36, n. 1, p. 314-323, 2010.

SCHNEIDER, C. A.; RASBAND, W. S.; ELICEIRI, K. W. **NIH imagem to ImageJ: 25 years of image analysis**. Nat. Meth., v. 9, n. 1, p. 671-675, 2012.

SHAO, N.; GAVRIILIDIS, A.; ANGELI, P. **Flow regimes for adiabatic gas-liquid flow in microchannels**. Chemical Engineering Science, v. 64, n. 1, p. 2749-2761, 2009.

SHAO, N.; SALMAN, W.; GAVRIILIDIS, A.; ANGELI, P. **CFD simulations of the effect of inlet conditions on Taylor flow formation**. International Journal of Heat and Fluid Flow, v. 29, n. 1, p. 1603-1611, 2008.

SOBIESZUK, P.; CYGANSKI, P.; POHORECKI, R. **Bubble lengths in the gas-liquid Taylor flow in microchannels**. Chemical Engineering Research and Design, v. 88, n. 1, p. 263-269, 2010.

STEFANOV, B. I.; KANEVA, N. V.; PUMA, G. L.; DUSHKIN, C. D. **Novel integrated reactor for evaluation of activity of supported photocatalytic thin films: Case of methylene blue degradation on TiO_2 and nickel modified TiO_2 under UV and visible light**. Colloids

and Surfaces A: Physicochemical and Engineering Aspects, v. 382, n. 1-3, p. 219-225, 2011.

SU, Y.; HESSEL, V.; NOËL, T. **A compact photomicroreactor design for kinetic studies of gas-liquid photocatalytic transformations**. AIChE Journal v. 61, n. 7, p. 2215-2227, 2015.

SU, Y.; KUIJPERS, K.; HESSEL, V.; NOËL, T. **A convenient numbering-up strategy for the scale-up of gas-liquid photoredox catalysis in flow**. Reaction Chemistry & Engineering, v. 1, n. 1, p. 73-81, 2016.

SU, Y.; STRAATHOF, N. J. W.; HESSEL, V.; NOËL, T. **Photochemical transformations accelerated in continuous-flow reactors: basic concepts and applications**. Chemistry – A European Journal, v. 20, n. 34, p. 10562-10589, 2014.

SU, Y.; TALLA, A.; HESSEL, V.; NOËL, T. **Controlled photocatalytic aerobic oxidation of thiols to disulfides in an energy-efficient photomicroreactor**. Chemical Engineering & Technology, v. 38, n. 10, p. 1733-1742, 2015.

SUO, M.; GRIFFITH, P. **Two-phase flow in capillary tubes**. Journal of Basic Engineering, v. 86, n. 1, p. 576-582, 1964.

THOME, J. R.; BAR-COHEN, A.; REVELLIN, R.; ZUN, I. **Unified mechanistic multiscale mapping of two-phase flow patterns in microchannels**. Experimental Thermal and Fluid Science, v. 44, n. 1, p. 1-22, 2013.

VAN GERVEN, T.; MUL, G.; MOULIJN, J.; STANKIEWICZ, A. **A review of intensification of photocatalytic processes**. Chemical Engineering and Processing: Process Intensification, v. 46, n. 9, p. 781-789, 2007.

VISAN, A.; RAFIEIAN, D.; OGIEGLO, W.; LAMMERTINK, R. G. H. **Modeling intrinsic kinetics in immobilized photocatalytic microreactors**. Applied Catalysis B: Environmental, v. 150-151, n. 1, p. 93-100, 2014.

WILLIAMS, G.; SEGER, B.; KAMAT, P. V. **TiO_2-graphene nanocomposites. UV-assisted photocatalytic reduction of graphene oxide.** ACS Nano, v. 2, n. 7, p. 1487-1491, 2008.

WÖRNER, M. **Numerical modeling of multiphase flows in microfluidics and micro process engineering: A review of methods and applications**. Microfluid Nanofluid, v. 12, n. 1, p. 841-886, 2012.

WU, C.- H.; CHERN, J.- M. **Kinetics of photocatalytic decomposition of methylene blue**. Industrial & Engineering Chemistry Research, v. 45, n. 19, p. 6450-6457, 2006.

WU, F.; LIU, W.; QIU, J.; *et al*. **Enhanced photocatalytic degradation and adsorption of methylene blue via TiO_2 nanocrystals supported on graphene-like bamboo charcoal**. Applied Surface Science, v. 358, part A, p. 425-435, 2015.

ZHANG, H.; LV, X.; LI, Y.; WANG, Y.; LI, J. **P25-graphene composite as a high performance photocatalyst**. ACS Nano, v. 4, n. 1, p. 380-386, 2010.